

Exploring the parameter space of MagLIF implosions using similarity scaling. I. Theoretical framework

D. E. Ruiz,^{1, a)} P. F. Schmit,² D. A. Yager-Elorriaga,¹ C. A. Jennings,¹ and K. Beckwith¹

¹⁾*Sandia National Laboratories, P.O. Box 5800, Albuquerque, NM 87185, USA*

²⁾*Lawrence Livermore National Laboratory, Livermore, CA 94550, USA*

(Dated: 25 November 2024)

Magneto-inertial fusion (MIF) concepts, such as the Magnetized Liner Inertial Fusion (MagLIF) platform [M. R. Gomez *et al.*, Phys. Rev. Lett. **113**, 155003 (2014)], constitute a promising path for achieving ignition and significant fusion yields in the laboratory. The space of experimental input parameters defining a MagLIF load is highly multi-dimensional, and the implosion itself is a complex event involving many physical processes. In the first paper of this series, we develop a simplified analytical model that identifies the main physical processes at play during a MagLIF implosion. Using non-dimensional analysis, we determine the most important dimensionless parameters characterizing MagLIF implosions and provide estimates of such parameters using typical fielded or experimentally observed quantities for MagLIF. We then show that MagLIF loads can be “incompletely” similarity scaled, meaning that the experimental input parameters of MagLIF can be varied such that many (but not all) of the dimensionless quantities are conserved. Based on similarity-scaling arguments, we can explore the parameter space of MagLIF loads and estimate the performance of the scaled loads. In the follow-up papers of this series, we test the similar scaling theory for MagLIF loads against simulations for two different scaling “vectors”, which include current scaling and rise-time scaling.

I. INTRODUCTION

For the last 60 years, one of the main approaches to produce thermonuclear self-heating plasmas has been laser-driven inertial confinement fusion (ICF).^{1,2} In this approach, powerful lasers directly or indirectly energize the outside surface of spherical capsules to achieve high ablation pressures (~ 100 Mbar) and implosion velocities greater than ~ 400 km/s. Recent experiments on the National Ignition Facility (NIF) have demonstrated hot-spot ignition using indirect drive.^{3–5} Given the limited energy that the NIF can deliver to a fuel capsule, hot-spot ignition attempts to minimize the required laser energy by igniting a central hot spot in the fuel, which then propagates into the dense outer fuel layer. However, hot-spot ignition places high engineering requirements on the manufacturing of the fuel capsule, on the design and delivery of the laser-pulse shape, and on the symmetry of the laser drive to maximize compression of the hot spot. As an alternative pathway to achieving ignition and high fusion yields in the laboratory, magneto-inertial fusion (MIF) relaxes these stringent implosion conditions by introducing strong magnetic fields, which modify the transport properties of the fuel and permit slower implosions.^{6–8} In particular, pulsed-power driven MIF is a technological approach that utilizes energy-rich, pulsed-power generators to compress a load configuration to thermonuclear conditions, albeit at a longer implosion timescale compared to laser-driven ICF.

One interesting MIF concept is the Magnetized Liner Inertial Fusion (MagLIF) platform, which is being studied at the Z Pulsed-Power Facility of Sandia National

Laboratories.^{9–15} The Z facility delivers a ~ 20 -MA current pulse to the cylindrical MagLIF load, which then implodes under the action of the $\mathbf{J} \times \mathbf{B}$ force.¹⁶ Since MagLIF employs a relatively thick and heavy metallic cylindrical tamper, or liner, the implosion velocities are 70–100 km/s, which are substantially lower than those in traditional ICF. Therefore, the fuel is not shock-heated; instead, it is preheated by a 2–4 kJ, TW-class laser to achieve sufficient adiabatic compression to fusion relevant temperatures.^{17–23} Since the implosions are slower (on the order of 100 ns), the fuel must be premagnetized to reduce thermal conduction losses.⁹ This is achieved by external electromagnetic coils that premagnetize the entire fuel volume with an axial 10–16 T magnetic field.¹⁶ The combination of these elements has led to thermonuclear yield production in laboratory experiments^{10,12,16} and significant plasma magnetization inferred via secondary DT neutron emission.^{24–26}

Pulsed-power driven MagLIF loads are complex systems that involve multiple processes that govern the electrical-circuit dynamics, liner-implosion dynamics, hydrodynamic instabilities, fuel-energy losses, particle transport, fuel-mass losses, axial magnetic-field transport, fusion yield, etc. Also, the experimental input parameters defining a MagLIF load are numerous. Main input parameters include: (i) the liner geometry (inner radius, outer radius, and height), (ii) the material composition of the liner, (iii) the preheat energy, (iv) the initial fuel density, (v) the external axial magnetic field, (vi) the peak current delivered to the load, and (vii) the rise time of the current waveform delivered to the load. Overall, the input-parameter space defining a MagLIF load is relatively high dimensional, and a detailed exploration of such space is therefore difficult.

Testing MagLIF performance in the entire input-parameter space is virtually impossible via integrated ex-

^{a)} Electronic mail: deruiz@sandia.gov

periments on Z. Radiation-hydrodynamic simulations offer an alternative to survey the performance of MagLIF, but such a study would still be computationally expensive when considering a large portion of the input-parameter space. Moreover, given the complexity of MagLIF implosions, there is also a level of uncertainty when surveying areas in parameter space that have not yet been experimentally fielded, even with today's highly complex multi-physics codes.^{9,11,17,20} The exploration of the parameter space for MagLIF can be simplified via the use of *dimensional analysis* and *similarity scaling*.

Our goal in this series of papers is to introduce a theoretical framework for similarity scaling MagLIF loads. This framework provides analytical scaling prescriptions for the main input parameters defining a MagLIF load and also gives estimates of performance of the resulting implosions. The theory also provides guidance on what simulations should be done and what experiments should be fielded on Z.

In Paper I of this series, we develop a simplified analytical model based on ordinary differential equations (ODEs) that contains the main physical processes at play during a MagLIF implosion. In many aspects, this model can be considered as a further reduced version of the ODE-based model presented in Refs. 27 and 28. After introducing the governing equations and writing them in dimensionless form, we determine the most important dimensionless parameters characterizing MagLIF implosions. We also provide estimates of such parameters using typical fielded or experimentally observed stagnation quantities for MagLIF. As originally demonstrated in Ref. 29, we then show that MagLIF loads can be *incompletely similarly scaled*, meaning that the experimental input parameters of MagLIF can be varied such that *many but not all* of the dimensionless quantities characterizing a MagLIF implosion are conserved. Following arguments based on similarity scaling, we can then estimate the performance of scaled MagLIF loads when using this framework.

Specific applications of these results are left to Refs. 30 and 31 (also referred as Papers II and III). In Paper II, we address the problem of scaling MagLIF loads with respect to the peak electrical current. In Paper III, we study the scaling MagLIF loads when the characteristic time of the voltage drive (or the current-rise time) is varied.

This paper can be divided into two (informal) parts. The first part comprises Secs. II–VIII, which discuss the main physical processes at play in a MagLIF implosion. In these sections, we identify the dimensionless parameters characterizing such processes. In Sec. III, we present a simplified two-layer liner model. In Sec. IV, we introduce a model for the liner in-flight aspect ratio, and we show how it can serve as a measure of the robustness of MagLIF liners towards the MRT instability. In Sec. V, we introduce a model describing the fuel energy balance. In Sec. VI, we discuss fuel mass losses as the liner implodes. In Sec. VII, we discuss the main processes at play during the flux compression of the axial magnetic field inside the

fuel. In Sec. VIII, we introduce the basic model for the fusion yield. In Sec. IX, we summarize the dimensionless parameters characterizing the identified main physical processes occurring in a MagLIF implosion and evaluate them using typical fielded or experimentally observed quantities for MagLIF.

The second part of this paper only comprises Sec. X. Here we discuss similarity scaling applied to MagLIF, and we introduce the notions of scale invariants, essential and non-essential dimensionless variables, and incomplete similarity scaling. We present the three major assumptions underlying the similarity-scaling framework applied to MagLIF and derive the general similarity-scaling prescriptions for the experimental input parameters characterizing a MagLIF configuration. A reader who is more interested in the application of similarity scaling to MagLIF may begin by reading Sec. X and then refer to the previous Secs. II–VIII for more details.

II. ELECTRICAL CIRCUIT MODEL

In contrast to laser-driven ICF, where the laser output is independent of the imploding spherical shell, magnetically-driven fusion loads, such as MagLIF, are inherently coupled to the pulsed-power driver delivering the current. Due to this dynamical coupling, it is necessary to model the dynamics of both the pulsed-power driver and the imploding load.

The Z Pulsed-Power Facility can be described using the equivalent circuit model shown in Fig. 1.^{27,32} The circuit is externally driven by a time-varying voltage $\varphi_{oc}(t)$, which is twice the forward-going voltage at the vacuum-insulator stack on Z, is independent of the load, and usually does not vary much between experiments for a given charge voltage. An example waveform for $\varphi_{oc}(t)$ is shown in Fig. 2.

For the left-most circuit loop in Fig. 1, the governing equation for the source current $I_s(t)$ is

$$L_0 \frac{d}{dt} I_s = \varphi_{oc} - Z_0 I_s - \varphi_c. \quad (1)$$

Here Z_0 is the effective impedance of the Z accelerator. L_0 and C respectively denote the inductance and capacitance of the magnetically-insulated transmission lines (MITLs). Finally, $\varphi_c(t)$ is the corresponding voltage across the capacitor C associated to the MITLs.

For the circuit loop located at the center of Fig. 1, the governing equation is

$$C \frac{d}{dt} \varphi_c = I_s - I_l - \frac{\varphi_c}{R_{\text{loss}}}, \quad (2)$$

where $I_l(t)$ is the electrical current going into the load region and $R_{\text{loss}}(t)$ is a shunt resistor used to model losses at the post-hole convolute.³³ Here we model the shunt resistor using a prescribed time-dependent model so that R_{loss} is given by

$$R_{\text{loss}}(t) \doteq R_{\text{loss},i} + (R_{\text{loss},f} - R_{\text{loss},i})f(t), \quad (3)$$

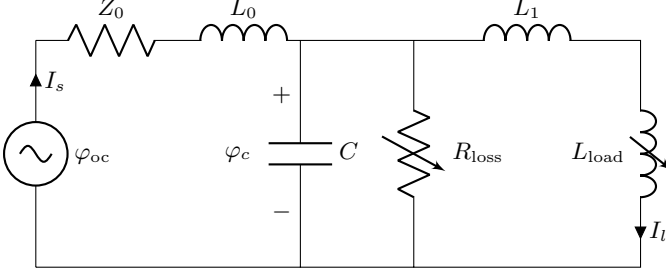


FIG. 1. Representative circuit diagram of the Z generator. Typical parameters used are $Z_0 = 0.18 \, \Omega$, $L_0 \simeq 8.34 \, \text{nH}$, $C \simeq 8.41 \, \text{nF}$, and $L_1 \simeq 5 \, \text{nH}$.

where

$$f(t) = \frac{1}{1 + \exp\left(-\frac{t - t_{\text{loss}}}{\Delta t_{\text{loss}}}\right)}. \quad (4)$$

is a function describing the transition from the initial loss resistance $R_{\text{loss},i}$ of the circuit early in time to the final loss resistance $R_{\text{loss},f}$ at later times. Typically, $R_{\text{loss},i} > R_{\text{loss},f}$ meaning that the fraction of current losses to the load increases as time progresses. In Eq. (4), t_{loss} represents the time at which current losses turn on, and Δt_{loss} is the characteristic time describing the transition in resistance of R_{loss} .

In Fig. 1, the load current I_l is determined by

$$\frac{d}{dt}(L_{\text{load}} I_l) + L_1 \frac{d}{dt} I_l = \varphi_c, \quad (5)$$

where L_1 is the initial, time-independent inductance of the feed region, which includes the post-hole convolute, the inner-MITL, and the return-can volume. $L_{\text{load}}(t)$ is the time-dependent inductance of the MagLIF liner. We approximate L_{load} as a coaxial inductance so that

$$L_{\text{load}}(t) \doteq \frac{\mu_0 h}{2\pi} \ln\left(\frac{R_{\text{out},0}}{R_{\text{out}}}\right), \quad (6)$$

where $R_{\text{out}}(t)$ is the liner outer radius, $R_{\text{out},0} \doteq R_{\text{out}}(0)$ is the initial outer radius, and h is the height of the imploding region of the liner. For the sake of simplicity, we consider the liner as perfectly conducting so the driving azimuthal magnetic field does not diffuse into the liner. Magnetic diffusion leads to Ohmic heating of the liner surface and adds a (small) additional inductance term associated to the magnetic flux contained in the liner region. The former acts as an energy source for the liner material and can modify its effective compressibility. A more detailed model that includes magnetic diffusion is provided in Ref. 27.

Let us now write the circuit equations (1)–(5) in dimensionless form and identify the dimensionless groups that characterize the system. We introduce the following

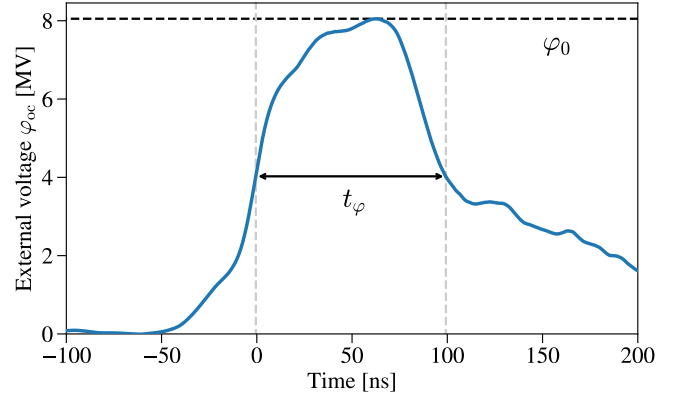


FIG. 2. Example of a voltage source φ_{oc} as a function of time. The characteristic voltage φ_0 can be taken as the maximum value of φ_{oc} . The characteristic time t_φ is defined as the full-width half-maximum (FWHM) of the voltage curve.

dimensionless variables:

$$\begin{aligned} \bar{t}_i &= \frac{t_i}{t_\varphi}, & \bar{I}_s &= \frac{I_s}{I_\star}, & \bar{I}_l &= \frac{I_l}{I_\star}, \\ \bar{\varphi}_{oc} &= \frac{\varphi_{oc}}{\varphi_0}, & \bar{\varphi}_c &= \frac{\varphi_c}{\varphi_0}, & \bar{R}_{\text{out}} &= \frac{R_{\text{out}}}{R_{\text{out},0}}. \end{aligned} \quad (7)$$

(From hereon, the “barred” quantities \bar{Q} denote dimensionless quantities.) Here φ_0 is the characteristic amplitude of the voltage source, which we define as the maximum voltage. The parameter t_φ represents the characteristic timescale of the voltage source. For pulsed-power systems, the maximum voltage and the duration of the voltage source near peak voltage are two key factors determining the current delivered to the load. We thus define t_φ as the full-width half-maximum (FWHM) of the voltage curve; e.g., see Fig. 2. In terms of the normalized voltage trace $\bar{\varphi}_{oc}(\bar{t})$, we can then write the external voltage source as $\varphi_{oc}(t) = \varphi_0 \bar{\varphi}_{oc}(t/t_\varphi)$. In Eq. (7), I_\star is the characteristic current of the circuit. To find a suitable expression for I_\star , we consider a short-circuit configuration in Fig. 1 with no dynamic load; i.e., $L_{\text{load}} = 0$. In the absence of the MITL capacitance C and current losses, the characteristic voltages across the voltage source φ_{oc} , the impedance Z_0 , and the inductors L_0 and L_1 satisfy

$$\varphi_0 \sim Z_0 I_\star + \frac{L_0 + L_1}{t_\varphi} I_\star. \quad (8)$$

Therefore, we define $I_\star \doteq \varphi_0 [Z_0 + (L_0 + L_1)/t_\varphi]^{-1}$, which in convenient units is written as

$$I_\star (\text{MA}) \doteq \frac{[\varphi_0 (\text{MV})]}{[Z_0 (\text{Ohm})] + \frac{[L_0 (\text{nH})] + [L_1 (\text{nH})]}{[t_\varphi (\text{ns})]}}. \quad (9)$$

Finally, t_i in Eq. (7) denotes the explicit time parameters appearing in Eqs. (1)–(5), such as t_{loss} and Δt_{loss} .

We substitute Eqs. (7) into Eqs. (1)–(5). The resulting

dimensionless equations are the following:

$$\frac{c_1}{1+c_2} \frac{d}{dt} \bar{I}_s = -\frac{c_2}{1+c_2} \bar{I}_s + \bar{\varphi}_{oc} - \bar{\varphi}_c, \quad (10)$$

$$c_3^2 \frac{d}{dt} \bar{\varphi}_c = \frac{\bar{I}_s - \bar{I}_l}{1+c_2} - \frac{\bar{\varphi}_c}{c_4 + (c_5 - c_4)f}, \quad (11)$$

$$(1 - c_1 - c_6 \ln \bar{R}_{out}) \frac{d}{dt} \bar{I}_l = c_6 \frac{\bar{I}_l}{\bar{R}_{out}} \frac{d\bar{R}_{out}}{dt} + (1 + c_2) \bar{\varphi}_c. \quad (12)$$

In terms of convenient units, the dimensionless parameters appearing in Eqs. (10)–(12) may be written as

$$c_1 \doteq \frac{[L_0(\text{nH})]}{[L_0(\text{nH})] + [L_1(\text{nH})]}, \quad (13)$$

$$c_2 \doteq \frac{[Z_0(\text{Ohm})] \cdot [t_\varphi(\text{ns})]}{[L_0(\text{nH})] + [L_1(\text{nH})]}, \quad (14)$$

$$c_3 \doteq \sqrt{[L_0(\text{nH})] + [L_1(\text{nH})]} \cdot \frac{[C(\text{nF})]^{1/2}}{[t_\varphi(\text{ns})]}, \quad (15)$$

$$c_4 \doteq \frac{[R_{loss,i}(\text{Ohm})] \cdot [t_\varphi(\text{ns})]}{[L_0(\text{nH})] + [L_1(\text{nH})]}, \quad (16)$$

$$c_5 \doteq \frac{[R_{loss,f}(\text{Ohm})] \cdot [t_\varphi(\text{ns})]}{[L_0(\text{nH})] + [L_1(\text{nH})]}, \quad (17)$$

$$c_6 \doteq \frac{\mu_0 h}{2\pi(L_0 + L_1)} = 2 \frac{[h(\text{cm})]}{[L_0(\text{nH})] + [L_1(\text{nH})]}. \quad (18)$$

The dimensionless parameters c_1 to c_6 characterize the circuit dynamics. In Eq. (13), the parameter c_1 is the ratio of the inductance L_0 of the outer MITLs and the total initial inductance of the “shorted circuit” ($L_0 + L_1$). This parameter measures the static-inductance matching between the pulsed-power driver and the initial feed inductance (convolute, inner MITL and load). The parameter c_2 in Eq. (14) is the ratio of the timescale t_φ of the voltage drive and the characteristic time $(L_0 + L_1)/Z_0$ of the pulsed-power generator. This parameter is a measure of the resonance between the voltage drive and the pulsed-power generator and serves as a good indicator of the driving efficiency. The parameter c_3 in Eq. (15) is the ratio of the time $\sqrt{(L_0 + L_1)C}$ and the characteristic time t_φ . This parameter measures the coupling of the circuit to the capacitance C of the MITLs; in other words, it describes how well the MITLs can capacitively store and release electrical energy into the circuit. The parameters c_4 and c_5 measure how efficient the current transmission is into the load region early and late in time. When c_4 or c_5 are large, there are negligible current losses; when c_4 or c_5 are small, current losses can be significant. Finally, the dimensionless parameter c_6 in Eq. (18) is related to the ratio of the time-dependent inductance of the imploding load and the initial total inductance of the circuit. Along with the parameter Π defined in Eq. (37) later on, c_6 characterizes the nonlinear coupling between the circuit and the imploding liner. When c_6 is large, the coupling is stronger which means that changes of the time-dependent inductance of an imploding load can significantly alter

the delivered current to the load. As shown in Eq. (18), coupling between the load and the pulsed-power generator increases when the imploding height h of the liner is large and when the initial total inductance ($L_0 + L_1$) of the circuit is small, which is the case of lower impedance pulsed-power machines.

III. LINER DYNAMICS

To describe the implosion of the liner, we introduce the following simple *two-layer* liner model. The governing equations for the inner and outer radii of the liner are

$$\frac{\hat{m}}{2} \frac{d^2}{dt^2} R_{out} = 2\pi R_{out} (p_{liner} - p_{mag,ext}), \quad (19)$$

$$\frac{\hat{m}}{2} \frac{d^2}{dt^2} R_{in} = 2\pi R_{in} (p_{fuel} + p_{mag,int} - p_{liner}). \quad (20)$$

Here $R_{out}(t)$ and $R_{in}(t)$ are the outer and inner radii of the liner, respectively. To each shell, we assign half of the liner mass per-unit-length \hat{m} ,³⁴ which is defined as

$$\hat{m} = \pi \rho_{liner,0} (R_{out,0}^2 - R_{in,0}^2), \quad (21)$$

where $\rho_{liner,0}$ is the initial mass density of the liner, $R_{out,0}$ is the initial liner outer radius, and $R_{in,0}$ is the initial liner inner radius. It is customary to use the liner aspect ratio

$$AR \doteq \frac{R_{out,0}}{\delta R_0} = \frac{R_{out,0}}{R_{out,0} - R_{in,0}} \quad (22)$$

where δR_0 is the initial liner thickness. For large initial AR liners, i.e., thin shells, the liner mass per-unit-length is approximately $\hat{m} \simeq 2\pi \rho_{liner,0} R_{out,0}^2 / AR$.

The liner is subject to the internal and external magnetic-field pressures, the internal pressure within the liner, and the pressure of the fuel inside the liner cavity. The external magnetic pressure $p_{mag,ext}(t)$ is given by

$$p_{mag,ext} \doteq \frac{B_\theta^2}{2\mu_0} = \frac{\mu_0 I_l^2}{8\pi^2 R_{out}^2}, \quad (23)$$

where $B_\theta(t)$ is the azimuthal magnetic field outside the liner generated by the load current I_l .

We assume that the internal pressure $p_{liner}(t)$ of the liner is solely determined by the mass density of the liner at a given time. In other words, we assume that the liner pressure obeys a cold adiabatic equation of state so that

$$p_{liner} \doteq p_{ref} \left(\frac{\rho_{liner}}{\rho_{ref}} \right)^\gamma = p_{ref} \left(\frac{\hat{m}/\rho_{ref}}{\pi(R_{out}^2 - R_{in}^2)} \right)^\gamma. \quad (24)$$

Here p_{ref} , ρ_{ref} , and γ are the reference pressure, mass density, and polytropic index that characterize the adiabatically compressed liner material. We note that, during a MagLIF implosion, the liner accesses diverse regions of the material-EOS phase space. The trajectories in the EOS phase space cannot be entirely described by the simple adiabatic-compression model (24) since a MagLIF

liner is usually shocked by the driving magnetic pressure early in the implosion. Moreover, the EOS phase-space trajectories depend on the liner-implosion dynamics and can change when scaling MagLIF loads. Although Eq. (24) has its limitations, we choose this model for the liner EOS in order to simplify the upcoming dimensional analysis. Revisions could be incorporated to include a more complete physics picture. For example, the predictive capability of the model could be increased by obtaining the parameters p_{ref} , ρ_{ref} , and γ from the regions in phase space that a MagLIF implosion accesses in more sophisticated material EOS models. Improvements such as this one will be left for future work.

In Eq. (20), $p_{\text{mag,int}}(t)$ denotes the magnetic pressure due to the flux-compressed axial magnetic field $B_z(t)$ within the fuel. It is given by

$$p_{\text{mag,int}} \doteq \frac{B_z^2}{2\mu_0}. \quad (25)$$

A model for $B_z(t)$ will be introduced in Sec. VII.

In Eq. (20), $p_{\text{fuel}}(t)$ denotes the internal pressure of the compressed fuel. We assume that the fuel is composed of an equimolar DT plasma so that the fuel pressure is

$$p_{\text{fuel}} = (1 + Z) \frac{\rho k_B T}{m_i} = \frac{2}{3} \frac{U}{\pi R_{\text{in}}^2 h}, \quad (26)$$

where $\rho(t)$ is the fuel mass density, $T(t)$ is the fuel temperature,³⁵ and $U(t)$ is the fuel internal energy. Also, k_B is the Boltzmann constant, $m_i \doteq Am_p$ is the ion mass, A is the average atomic number for the fusion fuel ($A = 2.5$ for equimolar DT plasma), m_p is the proton

mass, and Z is the charge number ($Z = 1$ for hydrogen-like fuel). Dynamical equations for U and ρ are derived in Secs. V and VI, respectively.

As a side note, it is common to describe imploding z-pinch liners as thin shells.^{29,36} The thin-shell model can be readily retrieved by summing Eqs. (19) and (20) and approximating $R(t) \simeq R_{\text{out}}(t) \simeq R_{\text{in}}(t)$. This leads to

$$\hat{m} \frac{d^2}{dt^2} R \simeq 2\pi R (p_{\text{fuel}} + p_{\text{mag,int}} - p_{\text{mag,ext}}). \quad (27)$$

This model is appropriate when the shell thickness $\delta R(t) \doteq R_{\text{out}}(t) - R_{\text{in}}(t)$ is much smaller than the outer or inner shell radii. For high-AR liners, it satisfactorily represents the initial dynamics of the implosion. However, it is no longer a good approximation near stagnation, when the liner thickness is almost equivalent to the liner outer radius; i.e., when $R_{\text{in}} \simeq 0$ and $R_{\text{out}} \simeq \delta R$.

We now determine the main dimensionless parameters characterizing the liner implosion. We introduce the following additional dimensionless variables:

$$\bar{R}_{\text{in}} \doteq \frac{R_{\text{in}}}{R_{\text{in},0}}, \quad \bar{p}_{\text{fuel}} \doteq \frac{p_{\text{fuel}}}{p_{\text{preheat}}}, \quad \bar{B}_z \doteq \frac{B_z}{B_{z,0}}, \quad (28)$$

where $B_{z,0}$ is the initial externally-applied axial magnetic field and p_{preheat} is the characteristic fuel pressure that is achieved after the end of the preheat stage. In terms of the initial liner dimensions and the total amount of energy E_{preheat} delivered to the fuel, p_{preheat} is given by

$$p_{\text{preheat}} \doteq \frac{2}{3} \frac{E_{\text{preheat}}}{\pi R_{\text{in},0}^2 h}. \quad (29)$$

In dimensionless form, Eqs. (19) and (20) become

$$\frac{1}{2} \frac{d^2 \bar{R}_{\text{out}}}{dt^2} = -\Pi \frac{\bar{I}_l^2}{\bar{R}_{\text{out}}} + 2\Lambda \bar{R}_{\text{out}} \left(\frac{\hat{m}/\rho_{\text{ref}}}{\pi R_{\text{out},0}^2} \right)^{\gamma-1} \left(\bar{R}_{\text{out}}^2 - \frac{R_{\text{in},0}^2}{R_{\text{out},0}^2} \bar{R}_{\text{in}}^2 \right)^{-\gamma}, \quad (30)$$

$$\frac{1}{2} \frac{d^2 \bar{R}_{\text{in}}}{dt^2} = \Phi \left(\frac{R_{\text{out},0}}{R_{\text{in},0}} \right)^2 \bar{R}_{\text{in}} \bar{p}_{\text{fuel}} + \Sigma \left(\frac{R_{\text{out},0}}{R_{\text{in},0}} \right)^2 \bar{R}_{\text{in}} \bar{B}_z^2 - 2\Lambda \bar{R}_{\text{in}} \left(\frac{\hat{m}/\rho_{\text{ref}}}{\pi R_{\text{out},0}^2} \right)^{\gamma-1} \left(\bar{R}_{\text{out}}^2 - \frac{R_{\text{in},0}^2}{R_{\text{out},0}^2} \bar{R}_{\text{in}}^2 \right)^{-\gamma}. \quad (31)$$

In this two-layer liner model, there are four important dimensionless parameters, which represent ratios of the various forms of energy relevant to MagLIF implosions:

$$\Pi \doteq \frac{\mu_0 I_\star^2}{4\pi \hat{m} R_{\text{out},0}^2 / t_\varphi^2} \sim \frac{\text{Magnetic potential energy}}{\text{Liner kinetic energy}}, \quad (32)$$

$$\Phi \doteq \frac{4}{3} \frac{E_{\text{preheat}}}{\hat{m} h R_{\text{out},0}^2 / t_\varphi^2} \sim \frac{\text{Preheat energy}}{\text{Liner kinetic energy}}, \quad (33)$$

$$\Lambda \doteq \frac{p_{\text{ref}}/\rho_{\text{ref}}}{R_{\text{out},0}^2 / t_\varphi^2} \sim \frac{\text{Liner internal energy}}{\text{Liner kinetic energy}}, \quad (34)$$

$$\Sigma \doteq \frac{\pi}{\mu_0} \frac{B_{z,0}^2 R_{\text{in},0}^2}{\hat{m} R_{\text{out},0}^2 / t_\varphi^2} \sim \frac{\text{Axial magnetic energy}}{\text{Liner kinetic energy}}. \quad (35)$$

The parameter Π represents a ratio of the characteristic magnetic potential energy to the liner kinetic energy. It denotes how strongly the magnetic drive accelerates the liner.³⁷ Larger Π values are associated with higher currents delivered to the load, longer timescales t_φ , less massive liners, and/or more compact liners. Along with the parameter c_6 in Eq. (18), Π characterizes the nonlinear dynamical coupling between the liner and the circuit. The dimensionless parameter Φ measures the relative im-

portance of the fuel internal energy to the liner kinetic energy. It characterizes the pushback done by the fuel on the imploding liner.²⁹ To increase Φ relative to Π , one clearly needs to increase the preheat per-unit-length

$$\hat{E}_{\text{preheat}} \doteq E_{\text{preheat}}/h. \quad (36)$$

The dimensionless quantity Λ characterizes the relative importance of the liner internal energy and is absent in the thin-shell model. This parameter is proportional to the ratio squared of the characteristic sound velocity $\sqrt{\gamma p_{\text{ref}}/\rho_{\text{ref}}}$ inside the liner and the characteristic implosion velocity ($\sim R_{\text{out},0}/t_\varphi$) of the liner. Finally, the last parameter Σ denotes the ratio of the energy associated with the axial magnetic field within the fuel and the liner kinetic energy. This parameter measures the amount of pushback of the flux-compressed axial magnetic field onto the liner. It is worth noting that the ratio Φ/Σ is effectively the ratio of the fuel pressure and the axial magnetic-field pressure, i.e., the well-known β parameter. In convenient units, these parameters are written as

$$\Pi = (10)^{-8} \frac{[I_\star(\text{MA})]^2 \cdot [t_\varphi(\text{ns})]^2}{[\hat{m}(\text{g/cm})] \cdot [R_{\text{out},0}(\text{cm})]^2}, \quad (37)$$

$$\Phi = \frac{4}{3} \cdot (10)^{-8} \frac{[E_{\text{preheat}}(\text{kJ})] \cdot [t_\varphi(\text{ns})]^2}{[\hat{m}(\text{g/cm})] \cdot [h(\text{cm})] \cdot [R_{\text{out},0}(\text{cm})]^2}, \quad (38)$$

$$\Lambda = (10)^{-6} \frac{[p_{\text{ref}}(\text{Mbar})] \cdot [t_\varphi(\text{ns})]^2}{[\rho_{\text{ref}}(\text{g/cm}^3)] \cdot [R_{\text{out},0}(\text{cm})]^2}, \quad (39)$$

$$\Sigma = \frac{5}{2} \cdot (10)^{-11} \frac{[B_{z,0}(\text{T})]^2 \cdot [R_{\text{in},0}(\text{cm})]^2 \cdot [t_\varphi(\text{ns})]^2}{[\hat{m}(\text{g/cm})] \cdot [R_{\text{out},0}(\text{cm})]^2}. \quad (40)$$

There are two other dimensionless factors appearing in Eqs. (30) and (31) that are of less importance. For high-AR liners, the dimensionless factor $\hat{m}/(\pi R_{\text{out},0}^2 \rho_{\text{ref}})$ is approximately written as

$$\frac{\hat{m}/\rho_{\text{ref}}}{\pi R_{\text{out},0}^2} \simeq \frac{\rho_{\text{liner},0}}{\rho_{\text{ref}}} \frac{2}{\text{AR}}. \quad (41)$$

Thus, it is a function of the material properties of the liner and its initial aspect ratio. The second dimensionless factor $(R_{\text{in},0}/R_{\text{out},0})^2$ depends on the liner geometry and can be rewritten as

$$\left(\frac{R_{\text{in},0}}{R_{\text{out},0}} \right)^2 \simeq 1 - \frac{2}{\text{AR}} \quad (42)$$

for high-AR liners.

The curious reader might wonder about the origins of the specific interpretation given to the parameters in Eqs. (37)–(40) and ask why the parameters in Eqs. (37)–(40) are more important than those in Eqs. (41) and (42). We can answer these questions following an energy-conservation argument. Let us multiply Eq. (30) by $d\bar{R}_{\text{out}}/d\bar{t}$ and Eq. (31) by $(R_{\text{in},0}/R_{\text{out},0})^2 d\bar{R}_{\text{in}}/d\bar{t}$. Summing the resulting equations and integrating leads to an energy-conservation equation:

$$\underbrace{-\Pi \int \frac{\bar{I}_l^2}{\bar{R}_{\text{out}}} d\bar{R}_{\text{out}}}_{\text{External magnetic energy extracted}} = \underbrace{\frac{1}{4} \left(\frac{R_{\text{in},0}}{R_{\text{out},0}} \right)^2 \left(\frac{d\bar{R}_{\text{in}}}{d\bar{t}} \right)^2 + \frac{1}{4} \left(\frac{d\bar{R}_{\text{out}}}{d\bar{t}} \right)^2}_{\text{Liner kinetic energy}} \underbrace{- \frac{\Phi}{2} \int \bar{p}_{\text{fuel}} d\bar{R}_{\text{in}}^2}_{\text{Work on fuel column}} \\ + \underbrace{- \frac{\Sigma}{2} \int \bar{B}_z^2 d\bar{R}_{\text{in}}^2}_{\text{Work on flux compressed } B_z} + \underbrace{\frac{\Lambda}{\gamma - 1} \left[\left(\frac{p_{\text{liner}}}{p_{\text{ref}}} \right)^{(\gamma-1)/\gamma} - \left(\frac{p_{\text{liner},0}}{p_{\text{ref}}} \right)^{(\gamma-1)/\gamma} \right]}_{\text{Work on compressed liner}}, \quad (43)$$

where we substituted Eq. (24). We have explicitly denoted the physical meaning of each term in Eq. (43). The quantity $p_{\text{liner},0}$ denotes the initial pressure within the liner, which is negligible. From Eq. (43), we conclude that the available magnetic energy extracted by the imploding liner is converted to liner kinetic energy, compression of the fuel column, flux-compression of the axial magnetic field, and compression of the liner itself. The main energy channels appearing in Eq. (43) are characterized by the four parameters given in Eqs. (37)–(40).

IV. LINER STABILITY AND ROBUSTNESS TO MRT INSTABILITIES

As discussed in Ref. 29, the MRT modes that most decrease the amount of pdV work done on the fuel and reduce confinement are those that maximize the perturbations at the liner interior surface. When accounting for MRT feedthrough, one can estimate the number of e -foldings of the most dangerous MRT modes during the acceleration phase of the implosion.²⁹

$$\Gamma_{\max}(t) \simeq \frac{1}{4} \frac{\text{IFAR}(t)}{R_{\text{out}}(t)} \left(\int_0^t \sqrt{|\ddot{R}_{\text{out}}|} dt' \right)^2, \quad (44)$$

where the liner in-flight aspect ratio (IFAR) is defined as the ratio of the imploding shell outer radius and the shell thickness:

$$\text{IFAR}(t) \doteq \frac{R_{\text{out}}(t)}{\delta R(t)} = \frac{R_{\text{out}}(t)}{R_{\text{out}}(t) - R_{\text{in}}(t)}. \quad (45)$$

Notably, $\text{IFAR}(0) = \text{AR}$, where AR is the initial liner aspect ratio. The IFAR is a commonly used metric in the ICF community to measure the stability of imploding shells.³⁸ In general, larger IFAR values indicate that the shells are more unstable to Rayleigh–Taylor instabilities.

Equation (44) serves as our measure of the resilience of the liner to the MRT instability. To maintain (or even improve) liner stability, one can *simultaneously* satisfy the following three conditions. First, one should avoid modes of operation requiring high convergence ratios [$\text{CR}_{\text{out}} \doteq R_{\text{out},0}/R_{\text{out}}(t)$] of the liner prior to deceleration. Second, the characteristic amplitude of the liner IFAR should not increase when changing the MagLIF load parameters. Third, the integral of the square root of the liner acceleration history should not increase when varying the liner parameters.

The liner IFAR can be calculated numerically when solving Eqs. (19) and (20). However, one can derive an approximate expression for the IFAR as follows. Subtracting Eqs. (19) and (20) gives

$$\frac{\hat{m}}{2} \frac{d^2 \delta R}{dt^2} = -2\pi [R_{\text{in}} p_{\text{fuel}} + R_{\text{in}} p_{\text{mag,int}} + R_{\text{out}} p_{\text{mag,ext}} - (R_{\text{out}} + R_{\text{in}}) p_{\text{liner}}]. \quad (46)$$

We assume that the left-hand side of Eq. (46) is negligible so that the liner pressure is in a quasi-equilibrium state. This effectively eliminates the high-frequency oscillations of the liner as it vibrates during the implosion. We then substitute $R_{\text{in}} = R_{\text{out}} - \delta R$ into Eq. (46). In the thin-shell limit, we neglect $\delta R/R_{\text{out}}$ terms on the right-hand side. As previously mentioned, this limit is valid as long as the liner has not converged too much. In the regime of validity of this approximation, the fuel pressure and internal magnetic pressure are small compared to the external magnetic pressure driving the implosion. Therefore, we may drop those terms. Next, we substitute Eq. (24) for the internal pressure of the liner and solve the resulting algebraic equation for δR . This gives

$$\text{IFAR}(t) \simeq 2\pi \frac{R_{\text{out}}^2(t) \rho_{\text{ref}}}{\hat{m}} \left(\frac{p_{\text{mag,ext}}(t)}{2p_{\text{ref}}} \right)^{1/\gamma}. \quad (47)$$

Equation (47) is in general agreement with the results derived in Refs. 29 and 39. In those works, a model for the IFAR was derived from a fluid-type momentum conservation equation for an imploding thin shell. Since the

starting point here is the two-layer liner model, there are discrepancies with the numerical coefficients, as well as the dependency on the ratio $p_{\text{fuel}}/p_{\text{mag}}$. However, more importantly for this work, the derived expression for the IFAR is proportional to $R_{\text{out}}^2 p_{\text{mag,ext}}^{1/\gamma} / \hat{m}$ as in Refs. 29 and 39.

In terms of dimensionless quantities, the number of e -foldings Γ_{\max} in Eq. (44) is written as

$$\Gamma_{\max}(\bar{t}) = \frac{1}{4} \frac{\text{IFAR}(\bar{t})}{\bar{R}_{\text{out}}(\bar{t})} \left(\int_0^{\bar{t}} \sqrt{|\ddot{\bar{R}}_{\text{out}}(\bar{t}')|} d\bar{t}' \right)^2. \quad (48)$$

We can also rewrite the liner IFAR in terms of dimensionless variables as follows:

$$\text{IFAR}(\bar{t}) = \Psi \bar{R}_{\text{out}}^2 \left(\frac{\bar{I}_l}{\bar{R}_{\text{out}}} \right)^{2/\gamma}, \quad (49)$$

where the dimensionless parameter Ψ represents the characteristic amplitude of the liner IFAR:

$$\Psi \doteq 2\pi \frac{[R_{\text{out},0}(\text{cm})]^{2-2/\gamma} \cdot [\rho_{\text{ref}}(\text{g/cm}^3)] \cdot [I_*(\text{MA})]^{2/\gamma}}{(200\pi)^{1/\gamma} \cdot [\hat{m}(\text{g/cm})] \cdot [p_{\text{ref}}(\text{Mbar})]^{1/\gamma}}. \quad (50)$$

Three factors contribute to the characteristic amplitude Ψ of the IFAR. First, Ψ depends on the initial geometry of the liner: the term R_{out}^2/\hat{m} is proportional to the initial aspect ratio (AR) of the liner. For this reason, the liner initial AR is often considered as a measure of liner robustness towards instabilities.⁹ Second, Ψ depends on the characteristic magnetic pressure acting on the liner, which is proportional to $(I_*/R_{\text{out},0})^2$. Higher magnetic pressures lead to larger values of the IFAR due to enhanced magnetic compression. Finally, Ψ depends on the compressibility of the liner, which manifests itself via the parameters ρ_{ref} , p_{ref} , and γ .

V. FUEL ENERGETICS

In a simplified manner, the energy-balance equation for the fuel is given by^{9,27}

$$\frac{dU}{dt} = P_{\text{preheat}} + P_{\text{pdV}} + P_{\alpha} - P_{\text{rad}} - P_{\text{c}} - P_{\text{end}} + P_{\text{other}}. \quad (51)$$

The right-hand side of Eq. (51) includes the various energy source and sink mechanisms present in a MagLIF implosion. $P_{\text{preheat}}(t)$ is the external fuel preheat rate, $P_{\text{pdV}}(t)$ is the pdV-work rate on the fuel, and $P_{\alpha}(t)$ is heating rate due to α particles. Regarding the energy-loss mechanisms, $P_{\text{rad}}(t)$ is the radiative cooling rate, $P_{\text{c}}(t)$ is the cooling rate due to conduction losses, and $P_{\text{end}}(t)$ represents an energy-loss rate due to mass flow through the open liner ends. Finally, $P_{\text{other}}(t)$ represents other energy source and loss mechanisms that are not discussed in this work; for example, additional radiation losses due to mixing of contaminants into the fuel ($P_{\text{other}} = -P_{\text{rad,mix}}$),¹³

degradation of the compressional pdV work caused by MRT instabilities ($P_{\text{other}} = -P_{\text{MRT}}$),³⁸ and recirculation of energy from ablation of the liner material caused by local heat fluxes ($P_{\text{other}} = P_c$).² In the remainder of this section, we shall discuss in further detail the terms appearing in Eq. (51).

A. Energy source and sink mechanisms

Fuel preheat. Before external preheat occurs, the internal gas pressure is negligible compared to the compressive magnetic pressure of the pulsed-power driver. Therefore, it is a good approximation to neglect the fuel internal energy prior to the laser preheat. Once laser preheat occurs, we assume that an energy E_{preheat} is instantaneously deposited uniformly into the fuel volume.⁴⁰ Within this approximation, we model the preheat rate as follows:

$$P_{\text{preheat}} \doteq E_{\text{preheat}} \delta(t - t_{\text{preheat}}), \quad (52)$$

where t_{preheat} is the time at which preheat occurs.

Compressional pdV work. After preheat, the imploding liner performs work onto the fuel gas in its interior. Therefore, the pdV work rate is given by

$$P_{\text{pdV}} \doteq -p_{\text{fuel}}(t) \frac{d}{dt} \pi R_{\text{in}}^2 h = -\frac{4}{3} \frac{U}{R_{\text{in}}} \frac{dR_{\text{in}}}{dt}, \quad (53)$$

where we substituted Eq. (26).

Alpha heating. In a self-heating scenario, the energetic α particles created by DT fusion reactions can be confined by the axial magnetic field B_z within the plasma. As the α particles collide with the fuel electrons, they lose their energy and heat the background fuel plasma. A simple expression for the α -heating rate is the following:⁴¹

$$P_{\alpha} = \varepsilon_{\alpha} \frac{dY}{dt} \eta_{\alpha}, \quad (54)$$

where $\varepsilon_{\alpha} = 3.5$ MeV is the energy of the α particles and dY/dt is the neutron-yield rate [see Eq. (106)]. The parameter $\eta_{\alpha}(t) \leq 1$ represents the fraction of α particles trapped within the fuel column. When assuming that α particles are primarily lost radially instead of axially, we may approximate the fraction η_{α} by⁴²

$$\eta_{\alpha} \simeq \frac{x_{\alpha} + x_{\alpha}^2}{1 + 13x_{\alpha}/9 + x_{\alpha}^2}, \quad (55)$$

where the dimensionless parameter x_{α} is defined as

$$x_{\alpha} \doteq \frac{8}{3} \left(\frac{R_{\text{in}}}{\ell_{\alpha}} + \frac{(R_{\text{in}}/\ell_{\alpha})^2}{\sqrt{9(R_{\text{in}}/\ell_{\alpha})^2 + 1000}} \right). \quad (56)$$

The parameter x_{α} depends on two dimensionless quantities. First, $R_{\text{in}}/\ell_{\alpha}$ is the ratio of the fuel-column radius

and the stopping length of the 3.5-MeV α particles. In terms of practical units, this dimensionless parameter is⁴³

$$\frac{R_{\text{in}}}{\ell_{\alpha}} = 9.34 \frac{\ln \Lambda_{\alpha e} \cdot [\rho R_{\text{in}} (\text{g/cm}^2)]}{[T (\text{keV})]^{3/2}}, \quad (57)$$

where $\ln \Lambda_{\alpha e}$ is the Coulomb logarithm for collisions between α particles and electrons. The parameter $R_{\text{in}}/\ell_{\alpha}$ is the ratio of the fuel-column radius R_{in} to the Larmor radius $\ell_{\alpha} \doteq v_{\alpha}/\Omega_{\alpha}$ of the 3.5-MeV α particles, where $v_{\alpha} \doteq \sqrt{2m_{\alpha}\varepsilon_{\alpha}}$ is their initial velocity, $\Omega_{\alpha} \doteq 2eB_z/m_{\alpha}$ is the gyrofrequency of α particles, e is the elementary charge, and m_{α} is the mass of an α particle. In convenient units, $R_{\text{in}}/\ell_{\alpha}$ can be written as

$$\frac{R_{\text{in}}}{\ell_{\alpha}} \doteq \frac{[B_z (\text{T})] \cdot [R_{\text{in}} (\text{cm})]}{26.5}. \quad (58)$$

When $R_{\text{in}}/\ell_{\alpha}$ becomes larger than unity, MagLIF transitions to a regime where many α particles are magnetically confined within the fuel plasma column. Note that $R_{\text{in}}/\ell_{\alpha}$ is proportional to the magnetic-field-radius product^{24,25} and can be inferred in present-day MagLIF experiments.²⁶ In MagLIF implosions, $R_{\text{in}}/\ell_{\alpha} \gg R_{\text{in}}/\ell_{\alpha}$, so magnetic confinement is the main mechanism for trapping α particles, not collisions.

Radiation losses. Electron Bremsstrahlung emission is the dominant mechanism for radiation losses. When assuming that the fuel plasma is optically thin and that any radiation energy deposited into the MagLIF liner does not alter the implosion dynamics, the approximate energy-loss rate of a hot, uniform, cylindrical plasma is⁴³

$$P_{\text{rad}} \doteq \frac{64}{3\sqrt{2\pi}} \left(\frac{e^2}{4\pi\epsilon_0} \right)^3 \frac{1}{m_e c^2 \hbar} \sqrt{\frac{k_B T}{m_e c^2}} \frac{Z^3 \rho^2}{m_i^2} \pi R_{\text{in}}^2 h, \quad (59)$$

where ϵ_0 is the vacuum permittivity, m_e is the electron mass, $\hbar \doteq h/(2\pi)$ is the Planck constant, and c is the speed of light. The factor $\pi R_{\text{in}}^2 h$ denotes the volume of the plasma column. Here we do not consider other sources of radiation emission such as those coming from impurity mixing in MagLIF.¹³ Considering the effects of additional sources and their scaling is left for future work.

Conduction losses. Thermal conduction is another mechanism by which the plasma can lose its energy. Due to the radial compression of z-pinch plasmas, thermal conduction losses will be dominated by thermal flux in the radial direction. Therefore, the energy loss rate due to electron and ion conduction is approximately given by

$$P_c \doteq 2\pi R_{\text{in}} h (\kappa_{ce} + \kappa_{ci}) \partial_r (k_B T) \simeq 2\pi h (\kappa_{ce} + \kappa_{ci}) k_B T, \quad (60)$$

where $\partial_r T \simeq T/R_{\text{in}}$. Here κ_{ce} and κ_{ci} correspond to the electron and ion thermal conductivities, respectively. Due to the relatively slow compression rate of MagLIF implosions compared to its laser-ICF counterparts, the cylindrical MagLIF plasmas must be axially magnetized in order to prevent excessive heat conduction losses.⁹ For

magnetized plasmas, the electron and ion thermal conductivities are respectively given by⁴⁴

$$\kappa_{ce} \doteq Z \frac{\rho}{m_i} \frac{k_B T}{m_e} \tau_e g_e(x_e), \quad (61)$$

$$\kappa_{ci} \doteq \frac{\rho}{m_i} \frac{k_B T}{A m_p} \tau_i g_i(x_i), \quad (62)$$

where

$$\tau_e \doteq \frac{3(4\pi\epsilon_0)^2 m_i \sqrt{m_e} (k_B T)^{3/2}}{4\sqrt{2}\pi Z^2 \rho e^4 \ln \Lambda}, \quad (63)$$

$$\tau_i \doteq \frac{3(4\pi\epsilon_0)^2 m_i^{3/2} (k_B T)^{3/2}}{4\sqrt{\pi} Z^4 \rho e^4 \ln \Lambda}. \quad (64)$$

are the electron-ion and ion-ion collision times, respectively, and $\ln \Lambda$ is the Coulomb logarithm.

In Eqs. (61) and (62), the functions g_e and g_i describe the dependence of the electron and ion thermal conductivities on the axial magnetic field B_z :⁴⁴

$$g_e(x_e) \doteq \frac{11.92 + 4.664x_e^2}{3.7703 + 14.79x_e^2 + x_e^4}, \quad (65)$$

$$g_i(x_i) \doteq \frac{2.645 + 2x_i^2}{0.677 + 2.70x_i^2 + x_i^4}. \quad (66)$$

where $x_e \doteq \Omega_e \tau_e$ and $x_i \doteq \Omega_i \tau_i$ are respectively the electron and ion Hall parameters. $\Omega_e \doteq eB/m_e$ and $\Omega_i \doteq ZeB/m_i$ are the electron and ion gyrofrequencies, respectively. In convenient units, the electron and ion Hall parameters for equimolar DT fuel are given by

$$x_e = 8.0 \cdot (10)^{-3} \frac{[T(\text{keV})]^{3/2} \cdot [B_z(\text{T})]}{\ln \Lambda \cdot [\rho(\text{g/cm}^3)]}, \quad (67)$$

$$x_i = 1.18 \cdot (10)^{-4} \frac{[T(\text{keV})]^{3/2} \cdot [B_z(\text{T})]}{\ln \Lambda \cdot [\rho(\text{g/cm}^3)]}. \quad (68)$$

The magnetization of electrons and ions varies throughout a MagLIF implosion. For example, assuming that the preheat energy is deposited uniformly within the fuel, one can estimate that the electrons are marginally magnetized ($x_e \simeq 1$) and the ions are unmagnetized ($x_i \ll 1$) for typical laser-preheat energies and gas-fill densities. (See Sec. IX for a summary of typical preheat conditions.) As the implosion progresses, the fuel becomes hotter and the axial magnetic field increases due to flux compression. Near stagnation, the electrons are highly magnetized ($x_e \gg 1$), and the ions are marginally magnetized ($x_i \simeq 1$). In these regimes, the functions g_e and g_i have the following asymptotic behaviors:

$$g_e(x_e) \sim \begin{cases} 0.81/x_e, & x_e \simeq 1 \\ 4.66/x_e^2, & x_e \gg 1 \end{cases} \quad (69)$$

$$g_i(x_i) \sim \begin{cases} 3.91, & x_i \ll 1 \\ 1.06/x_i, & x_i \simeq 1 \end{cases} \quad (70)$$

Near stagnation, the dependence of g_i with the inverse of the ion Hall parameter x_i suggests that the ion thermal transport is in a Bohm-like regime.

End losses. Cylindrical MagLIF liners contain openings at their ends to inject fuel and preheat energy. Once the implosion is underway, hot fuel can leave the liner interior through these openings and take energy along with it. Following Refs. 9 and 27, we model the escape of fuel across the top and bottom openings as a rarefaction wave propagating to the interior of the fuel. According to Appendix A, the energy end losses are given by

$$P_{\text{end}} \simeq 0.90 \frac{U c_s R_c^2}{R_{\text{in}}^2 h} = 1.35\pi(1+Z) \frac{\rho k_B T}{m_i} c_s R_c^2, \quad (71)$$

where

$$c_s \doteq \sqrt{(1+Z)\gamma_{\text{fuel}} \frac{k_B T}{m_i}} \quad (72)$$

is the hydrodynamic (ion) sound speed and $\gamma_{\text{fuel}} = 5/3$. Also, $R_c(t)$ denotes the radius of the opening through which the fuel escapes the fluid. It is given by the minimum between the radius R_{LEH} of the laser-entrance-hole (LEH) window²⁰ and the liner inner radius. More specifically, $R_c(t) \doteq \min\{R_{\text{LEH}}, R_{\text{in}}(t)\}$.

B. Generalized equation-of-state for the fusion fuel

One can rewrite the differential equation (51) as an integral equation that makes more explicit the effects of energy sources and sinks. Substituting Eq. (52) and (53) into Eq. (51) and integrating in time gives the following:

$$\frac{U R_{\text{in}}^{4/3}}{E_{\text{preheat}} R_{\text{in,preheat}}^{4/3}} = \exp \left(\int_{t_{\text{preheat}}}^t \frac{P_\alpha - P_{\text{rad}} - P_c - P_{\text{end}}}{U} dt' \right), \quad (73)$$

where $R_{\text{in,preheat}} \doteq R_{\text{in}}(t_{\text{preheat}})$ is the liner inner radius at the moment of preheat. To maximize pdV work, $R_{\text{in,preheat}}$ is typically close to $R_{\text{in},0}$.

Equation (73) serves as a generalized equation of state (EOS) for the fuel internal energy. The form of this equation is reminiscent to that of previous works aimed at understanding the effects of α heating and of hydrodynamical instabilities on fuel compression.^{2,38,45} The interpretation of Eq. (73) is simple: in the absence of energy sources or sinks, the left-hand side of Eq. (73) represents perfect adiabatic compression of the fuel. The exponential on the right-hand side represents deviations from ideal adiabatic compression, i.e., changes in the entropy of the fuel.² When the argument of the exponential is positive (i.e., in the case of robust α heating), the internal energy of the fuel is larger than the purely adiabatic result at fixed inner convergence ratio $\text{CR}_{\text{in}} \doteq R_{\text{in},0}/R_{\text{in}}$. In the opposite case, when loss mechanisms are dominant, the fuel compression becomes less efficient: to achieve the same fuel internal energy at fixed E_{preheat} , the required inner convergence ratio must be larger.

The energy-source term corresponding to α heating in Eq. (73) is related to the general Lawson-criterion parameter χ for steady-state thermonuclear ignition that is often found in the ICF literature:⁴⁶

$$\begin{aligned}\chi &\doteq \int_{t_{\text{preheat}}}^t \frac{P_\alpha}{U} dt' \\ &= \int_{t_{\text{preheat}}}^t \frac{1}{6} \varepsilon_\alpha n_i^2 \frac{\langle \sigma v \rangle}{p_{\text{fuel}}} \eta_\alpha dt' \\ &= \int_{t_{\text{preheat}}}^t \frac{1}{24} \varepsilon_\alpha p_{\text{fuel}} \frac{\langle \sigma v \rangle}{(k_B T)^2} \eta_\alpha dt'.\end{aligned}\quad (74)$$

where we substituted Eqs. (26) and (106). Of course, significant neutron-yield production occurs during a relatively small window of time, known as the burn-width time τ_{bw} , which is small compared to the implosion time of the liner. (In practice, τ_{bw} is defined as the full-width half-maximum of the neutron-production rate.) In terms of convenient units, χ can be written as

$$\chi = 0.09 [p_{\text{fuel}} (\text{Gbar})] \cdot [\tau_{\text{bw}} (\text{ns})] \frac{[\langle \sigma v \rangle (10^{-18} \text{cm}^3/\text{s})]}{[T (\text{keV})]^2} \eta_\alpha. \quad (75)$$

Note that other Lawson parameters appearing in the ICF literature invoke a spatial average of the $\langle \sigma v \rangle / T^2$ over the fuel volume.⁴⁶ We do not have such spatial averaging due to the zero-dimensional nature of the model presented in this paper, but the expression in Eq. (75) could be readily improved so that the spatial-averaging operation is taken into account. It is also worth noting that, absent any energy-recycling mechanism^{2,45} potentially occurring from ablation of the liner inner surface, Eq. (75) includes the fraction $\eta_\alpha \leq 1$ of trapped α particles.

The generalized EOS (73) for the fusion fuel also provides insights on how the energy gain and loss mechanisms behave as the MagLIF liner implodes. For the following calculations in this section, we consider that the quantities describing the fuel and axial magnetic field are adiabatically compressed to leading order when neglecting non-ideal mechanisms. In terms of the inner convergence ratio $\text{CR}_{\text{in}} \doteq R_{\text{in},0}/R_{\text{in}} = 1/\bar{R}_{\text{in}}$, the parameters describing the fuel column behave as follows: $R_{\text{in}} \sim \text{CR}_{\text{in}}^{-1}$, $U \sim \text{CR}_{\text{in}}^{4/3}$, $\rho \sim \text{CR}_{\text{in}}^2$, $T \sim \text{CR}_{\text{in}}^{4/3}$, and $B_z \sim \text{CR}_{\text{in}}^2$. When substituting the power-law expression (109) for the DT reactivity into χ , we find that the relative energy-gain rate due to α heating grows as

$$\frac{1}{\tau_{\text{E},\alpha}} \doteq \frac{P_{\text{rad}}}{U} \sim \text{CR}_{\text{in}}^{5.69}, \quad (76)$$

where $\tau_{\text{E},\alpha}$ is the characteristic energy-gain time due to α heating. (In the calculation above, we ignored the effects of η_α which increases for larger CR_{in} values.) As expected, α heating is a process that rapidly increases near peak compression.

The relative radiation-loss rate behaves as

$$\frac{1}{\tau_{\text{E},\text{rad}}} \doteq \frac{P_{\text{rad}}}{U} \sim \text{CR}_{\text{in}}^{4/3}, \quad (77)$$

where $\tau_{\text{E},\text{rad}}$ is a characteristic energy confinement time due to radiation losses alone. Thus, relative energy losses due to radiation increase sharply as the implosion progresses towards stagnation.

Depending on the magnetization regime of electrons and ions, we have the following dependencies for thermal-conduction losses:

$$\frac{1}{\tau_{\text{E},\text{ce}}} \doteq \frac{P_{\text{ce}}}{U} \sim \begin{cases} \text{CR}_{\text{in}}^{4/3}, & \text{marginally magnetized} \\ \text{CR}_{\text{in}}^{-2/3}, & \text{strongly magnetized} \end{cases} \quad (78)$$

$$\frac{1}{\tau_{\text{E},\text{ci}}} \doteq \frac{P_{\text{ci}}}{U} \sim \begin{cases} \text{CR}_{\text{in}}^{10/3}, & \text{unmagnetized} \\ \text{CR}_{\text{in}}^{4/3}, & \text{marginally magnetized} \end{cases} \quad (79)$$

where $\tau_{\text{E},\text{ce}}$ and $\tau_{\text{E},\text{ci}}$ are characteristic energy confinement times due to electron and ion conduction losses, respectively. Here we used, $x_{e,i} \propto \text{CR}_{\text{in}}^2$. As shown in Eq. (78), electron thermal-conduction losses increase momentarily after the fuel preheat occurs, but once electrons become sufficiently magnetized, these losses saturate or become weaker as the implosion progresses. In contrast, ion thermal-conduction losses are expected to increase as the implosion progresses.

The characteristic energy-confinement time due to end losses depends on the inner convergence ratio as

$$\frac{1}{\tau_{\text{E},\text{end}}} \doteq \frac{P_{\text{end}}}{U} \sim \text{CR}_{\text{in}}^{2/3}. \quad (80)$$

The relative end-loss rate $1/\tau_{\text{E},\text{end}}$ climbs at a slower rate than its radiation and ion-conduction counterparts, which means that its effects on the degradation of the ideal compression of the fuel are more distributed in time from the moment of preheat to stagnation.

Finally, the total energy confinement time due to gains and losses can be defined as

$$\frac{1}{\tau_E} \doteq \frac{1}{\tau_{\text{E},\text{rad}}} + \frac{1}{\tau_{\text{E},\text{ce}}} + \frac{1}{\tau_{\text{E},\text{ci}}} + \frac{1}{\tau_{\text{E},\text{end}}} - \frac{1}{\tau_{\text{E},\alpha}}. \quad (81)$$

Tracking the ratio of the burn width τ_{bw} and τ_E (along with its individual components) can serve as a good measure of how the energy gain and loss mechanisms vary when studying different MagLIF configurations.

As a final concluding remark for this section, we wrote Eq. (73) as a generalized EOS for the fuel internal energy U . However, a similar expression can be derived for the fuel pressure p_{fuel} . Substituting Eq. (26) into Eq. (73) leads to an equation similar to Eq. (73) with U/E_{preheat} replaced by $p_{\text{fuel}}/p_{\text{preheat}}$ and the exponent $4/3$ changed to $10/3$. To obtain a generalized EOS for the fuel temperature, one can substitute Eq. (26) into Eq. (73) and also use the result in Eq. (91) to account for fuel-mass losses.

C. Dimensionless form

We shall now write Eq. (73) in dimensionless form. We introduce the following two dimensionless variables:

$$\bar{\rho} \doteq \frac{\rho}{\rho_0}, \quad \bar{T} \doteq \frac{T}{T_{\text{preheat}}}, \quad (82)$$

$$\bar{U} = \frac{\text{CR}_{\text{in}}^{4/3}}{\text{CR}_{\text{in,preheat}}^{4/3}} \exp \left[\int_{\bar{t}_{\text{preheat}}}^{\bar{t}} \left(\Upsilon_{\alpha} \bar{\rho} \bar{T}^{2.77} \eta_{\alpha} - \Upsilon_{\text{rad}} \frac{\bar{\rho}}{\bar{T}^{1/2}} - \Upsilon_{\text{ce}} \frac{\bar{T}^{5/2}}{\bar{\rho} \bar{R}_{\text{in}}^2} \frac{g_e(x_e)}{g_e(x_{e0})} - \Upsilon_{\text{ci}} \frac{\bar{T}^{5/2}}{\bar{\rho} \bar{R}_{\text{in}}^2} \frac{g_i(x_i)}{g_i(x_{i0})} - \Upsilon_{\text{end}} \frac{\bar{T}^{1/2} \bar{R}_c^2}{\bar{R}_{\text{in}}^2} \right) d\bar{t} \right], \quad (84)$$

where $\text{CR}_{\text{in,preheat}}$ is the inner convergence ratio at the moment of preheat and is usually close to unity (to maximize pdV work done on the fuel). In Eq. (84), we also used the approximate power-law expression (109) for the fusion reactivity. The quantities x_{e0} and x_{i0} denote the electron and ion Hall parameters evaluated at the characteristic plasma conditions. The dimensionless parameters Υ_{α} , Υ_{rad} , Υ_{ce} , Υ_{ci} , and Υ_{end} characterize the main energy source and loss mechanisms. For equimolar DT plasmas, these parameters are

$$\Upsilon_{\alpha} \doteq 0.002 [\rho_0(\text{g/cm}^3)] \cdot [T_{\text{preheat}}(\text{keV})]^{2.77} \cdot [t_{\varphi}(\text{ns})], \quad (85)$$

$$\Upsilon_{\text{rad}} \doteq 0.27 \frac{[\rho_0(\text{g/cm}^3)] \cdot [t_{\varphi}(\text{ns})]}{[T_{\text{preheat}}(\text{keV})]^{1/2}}, \quad (86)$$

$$\Upsilon_{\text{ce}} \doteq 5.3 \cdot (10)^{-5} \frac{[T_{\text{preheat}}(\text{keV})]^{5/2} \cdot [t_{\varphi}(\text{ns})] \cdot g_e(x_{e0})}{\ln \Lambda \cdot [\rho_0(\text{g/cm}^3)] \cdot [R_{\text{in},0}(\text{cm})]^2}, \quad (87)$$

$$\Upsilon_{\text{ci}} \doteq 7.9 \cdot (10)^{-7} \frac{[T_{\text{preheat}}(\text{keV})]^{5/2} \cdot [t_{\varphi}(\text{ns})] \cdot g_i(x_{i0})}{\ln \Lambda \cdot [\rho_0(\text{g/cm}^3)] \cdot [R_{\text{in},0}(\text{cm})]^2}, \quad (88)$$

$$\Upsilon_{\text{end}} \doteq 0.032 \frac{[T_{\text{preheat}}(\text{keV})]^{1/2} \cdot [t_{\varphi}(\text{ns})]}{[h(\text{cm})]}. \quad (89)$$

These dimensionless parameters have different dependencies on the parameters describing the plasma fuel conditions ($R_{\text{in},0}$, ρ_0 , $B_{z,0}$, E_{preheat} , and h). For example, Υ_{α} and Υ_{rad} are linearly dependent on the fuel density at fixed temperature. (In the high magnetization limit, Υ_{ce} is also linear with plasma density.) The parameters Υ_{ce} and Υ_{ci} have different power dependencies on the magnetic field B_0 when accounting for the magnetization regimes of the electrons and ions. For example, near stagnation, $g_e \sim x_e^{-2}$ and $g_i \sim x_i^{-1}$, which leads to $\Upsilon_{\text{ce}} \propto B_0^{-2}$ and $\Upsilon_{\text{ci}} \propto B_0^{-1}$. Finally, only the end-loss parameter Υ_{end} depends on the liner height h .

Equations (85)–(89) may be helpful to evaluate the tradeoffs when making small changes to the input parameters of experimentally fielded MagLIF loads. As

where $\rho_0 \doteq \rho(0)$ is the initial fuel mass density and

$$k_B T_{\text{preheat}} \doteq \frac{p_{\text{preheat}}}{(1+Z)(\rho_0/m_i)} \quad (83)$$

is the characteristic temperature of the fuel achieved after the preheat stage. When substituting Eqs. (26), (28) and (82) into Eq. (73), we obtain

an example, when substituting Eq. (83) into Eqs. (85)–(89), one finds that the parameters Υ_{ci} and Υ_{end} increase with T_{preheat} and therefore \hat{E}_{preheat} . Although increasing preheat will increase the initial adiabat of the fuel, this will not necessarily always lead to better performance for a MagLIF load since the relative loss rates due to ion-conduction and end flows increase. Therefore, to make best use of gains in preheat energy delivery to MagLIF loads, one must also increase the magnetic field $B_{z,0}$ and the liner height h so that ion-conduction losses and end-losses remain constant.

VI. FUEL MASS LOSSES

MagLIF liners are open-ended to allow entry of the laser to preheat the fuel. As the liner implodes, fuel mass can escape the imploding region of the liner. As was done in Sec. V A, the loss of fuel is modeled as a rarefaction wave. Following Appendix A, we obtain

$$\frac{d\rho}{dt} \simeq -2\rho \frac{1}{R_{\text{in}}} \frac{dR_{\text{in}}}{dt} - 0.63 \frac{\rho c_s R_c^2}{R_{\text{in}}^2 h}, \quad (90)$$

which agrees with expressions reported in Refs. 9 and 27 (modulo some minor numerical coefficients). The first term in Eq. (90) represents the adiabatic compression of the fuel. The second term describes the degradation of adiabatic compression due to fuel escaping the liner. As was done in Sec. V, Eq. (90) can be integrated in order to get a generalized EOS for the fuel density:

$$\frac{\rho(t) R_{\text{in}}^2}{\rho_0 R_{\text{in},0}^2} = \exp \left(-0.63 \int_{\text{preheat}}^t \frac{c_s}{h} \frac{R_c^2}{R_{\text{in}}^2} dt' \right), \quad (91)$$

where $\rho_0 \doteq \rho(0)$ is the initial fuel mass density. In the absence of fuel losses, the left-hand side of Eq. (91) denotes the increase of the fuel density with CR_{in} due to mass conservation. When the liner has sufficiently imploded so that $R_c = R_{\text{in}}$, mass end losses are mainly determined by the ratio of the distance traveled by a characteristic sound wave ($\int^t c_s dt$) and the liner imploding height h .

Since c_s behaves approximately as $\text{CR}_{\text{in}}^{2/3}$ to lowest order, the argument of the exponent is a relatively weak function of CR_{in} . Hence, fuel-mass losses are distributed in time throughout the implosion.

In terms of dimensionless variables, Eq. (91) becomes

$$\bar{\rho} = \text{CR}_{\text{in}}^2 \exp \left(-0.70 \int^{\bar{t}} \Upsilon_{\text{end}} \frac{\bar{T}^{1/2} \bar{R}_{\text{c}}^2}{\bar{R}_{\text{in}}^2} d\bar{t}' \right), \quad (92)$$

where Υ_{end} is given in Eq. (89). Not surprisingly, the dimensionless parameter Υ_{end} characterizes both energy and fuel-mass end losses. In accordance to simple physical intuition, increasing the initial fuel temperature (for example, by increasing preheat) or making the liner implosions slower and longer in time will increase fuel mass losses. To reduce relative end losses, the liner height h must be increased.

VII. MAGNETIC FIELD TRANSPORT

To obtain an evolution equation for the axial magnetic field, we start from the extended-magnetohydrodynamics induction equation. When neglecting the Hall term and the Biermann-battery term, we have⁴⁷

$$\frac{\partial \mathbf{B}}{\partial t} = \nabla \times (\mathbf{v} \times \mathbf{B}) + \nabla \times (D_M \nabla \times \mathbf{B}) + \frac{1}{e} \nabla \times \mathbf{F}_T, \quad (93)$$

where

$$D_M \doteq \frac{m_e \nu_{ei}}{n_e e^2 \mu_0} \quad (94)$$

is the magnetic diffusivity (assumed isotropic), $n_e \doteq Z \rho_i / m_i$ is the electron density, and

$$\mathbf{F}_T \doteq -\beta_{\parallel}^{uT} \nabla_{\parallel} k_B T - \beta_{\perp}^{uT} \nabla_{\perp} k_B T - \beta_{\Lambda}^{uT} \mathbf{e}_B \times \nabla k_B T \quad (95)$$

is the thermal force. Here β_{\parallel}^{uT} , β_{\perp}^{uT} , and β_{Λ}^{uT} are transport coefficients of the magnetic field [see Eq. (4.31) of Ref. 44]. The ∇_{\parallel} and ∇_{\perp} operators are gradients along and perpendicular to the magnetic field.

In MagLIF implosions, axial gradients are typically negligible when compared to radial gradients. Therefore, when spatially integrating Eq. (93) on an axial cross-section and applying Stokes theorem, we obtain

$$\frac{dB_z}{dt} \simeq -2 \frac{B_z}{R_{\text{in}}} \frac{dR_{\text{in}}}{dt} - 2B_z \frac{D_M}{R_{\text{in}}^2} - 2 \frac{\beta_{\Lambda}^{uT}}{e R_{\text{in}}^2} k_B T, \quad (96)$$

where we used $\partial_r B_z \simeq B_z / R_{\text{in}}$ and $\partial_r T \simeq T / R_{\text{in}}$. The first term on the right-hand side describes ideal flux compression. The second and third terms represent losses due to magnetic diffusion and Nernst advection. The transport coefficient β_{Λ}^{uT} is given by⁴⁴

$$\beta_{\Lambda}^{uT} \doteq x_e \frac{3.053 + 1.5x_e^2}{3.7703 + 14.79x_e + x_e^4}. \quad (97)$$

Depending on the value of the electron Hall parameter x_e , β_{Λ}^{uT} can be fitted according to the following power-law functions:

$$\beta_{\Lambda}^{uT}(x_e) \simeq \begin{cases} 0.810x_e, & x_e \ll 1 \\ 0.232, & 0.5 \leq x_e \leq 4 \\ 0.472/x_e^{1/2}, & 4 < x_e \leq 10 \\ 1.5/x_e, & x_e \geq 10 \end{cases} \quad (98)$$

Integrating Eq. (96), we obtain a generalized EOS for the axial magnetic field

$$\frac{B_z(t) R_{\text{in}}^2}{B_{z,0} R_{\text{in},0}^2} = \exp \left[-2 \int \left(\frac{D_M}{R_{\text{in}}^2} + \frac{\beta_{\Lambda}^{uT} k_B T}{e R_{\text{in}}^2 B_z} \right) dt \right]. \quad (99)$$

When magnetic diffusion and Nernst advection are negligible, $B_z(t) R_{\text{in}}^2 = B_{z,0} R_{\text{in},0}^2$, which is the frozen-in law for ideal MHD. When magnetic diffusion and Nernst advection become important, they hinder the ability of the plasma to flux compress the magnetic field. In a more sophisticated model that includes radial distributions of the fuel and magnetic-field quantities, magnetic diffusion and Nernst advection modify the distribution of the axial magnetic field within the fuel and typically decrease the magnetic thermal insulation of the fuel hot spot. When assuming an adiabatic compression of the parameters describing the fuel plasma (similar to the calculations in Sec. VB), we find that the Nernst-advection rate follows

$$\frac{\beta_{\Lambda}^{uT} k_B T}{e R_{\text{in}}^2 B_z} \sim \begin{cases} \text{CR}^{10/3}, & x_e \ll 1 \\ \text{CR}^{4/3}, & 0.5 \leq x_e \leq 4 \\ \text{CR}^{1/3}, & 4 < x_e \leq 10 \\ \text{CR}^{-2/3}, & x_e \geq 10 \end{cases} \quad (100)$$

Thus, magnetic-flux losses due to Nernst advection increase early in the implosion but decrease late in the implosion. Repeating the analysis for the magnetic-field diffusion term, we find that magnetic field is diffused uniformly throughout the implosion:

$$\frac{D_M}{R_{\text{in}}^2} \sim \text{const.} \quad (101)$$

In terms of dimensionless variables, Eq. (99) becomes

$$\bar{B} = \text{CR}_{\text{in}}^2 \exp \left[- \int^{\bar{t}} \left(\frac{\text{Md}}{\bar{T}^{3/2} \bar{R}_{\text{in}}^2} + \text{Ne} \frac{\bar{T}}{\bar{B}_z \bar{R}_{\text{in}}^2} \frac{\beta_{\Lambda}^{uT}(x_e)}{\beta_{\Lambda}^{uT}(x_{e0})} \right) d\bar{t}' \right], \quad (102)$$

where the dimensionless parameters describing the effects of magnetic diffusion and Nernst advection are

$$\text{Md} \doteq 5.19 \cdot (10)^{-8} \frac{\ln \Lambda \cdot [t_{\varphi}(\text{ns})]}{[T_{\text{preheat}}(\text{keV})]^{3/2} \cdot [R_{\text{in},0}(\text{cm})]^2}, \quad (103)$$

$$\text{Ne} \doteq 0.02 \frac{[T_{\text{preheat}}(\text{keV})] \cdot [t_{\varphi}(\text{ns})]}{[B_{z,0}(\text{T})] \cdot [R_{\text{in},0}(\text{cm})]^2} \beta_{\Lambda}^{uT}(x_{e0}). \quad (104)$$

It is interesting to note that the expression for Ne may elucidate some trends that are observed in experiments. MagLIF experiments^{16,26} suggest that the

magnetic-field-radius product $B_z R_{\text{in}}$ decreases when increasing the preheat energy. It was hypothesized that Nernst advection was the primary driver for this effect. If we admit that that Nernst advection is strongest within the mid-to-high magnetization regime shown in Eq. (98), the Ne parameter is approximated by

$$\text{Ne} \simeq 0.1 \frac{\ln \Lambda^{1/2} [\rho_0 (\text{g/cm}^3)]^{1/2} \cdot [T_{\text{preheat}} (\text{keV})]^{1/4} \cdot [t_\varphi (\text{ns})]}{[B_{z,0} (\text{T})]^{3/2} \cdot [R_{\text{in},0} (\text{cm})]^2}. \quad (105)$$

The Nernst parameter increases with the fuel temperature (or preheat energy) and with the fuel density, meaning that Nernst advection and magnetic-flux losses become stronger. The present dimensional analysis for Nernst advection seems to agree with the observed trend, but more careful analysis such as that in Ref. 48 is needed to verify this claim. This will be left for future work.

VIII. FUSION YIELD

For equimolar DT fuel, the neutron yield rate is approximately⁴³

$$\frac{dY}{dt} = \frac{1}{4} \left(\frac{\rho}{m_i} \right)^2 \langle \sigma v \rangle_{\text{DT}} \pi R_{\text{in}}^2 h, \quad (106)$$

where $\langle \sigma v \rangle(T)$ is the fusion reactivity. The Bosch-Hale expression for the fusion-reaction rate of DT plasma is⁴⁹

$$\langle \sigma v \rangle_{\text{DT}} = C_1 \frac{\xi^2}{\xi^{5/6}} \exp(-3\xi^{1/3}\xi), \quad (107)$$

where $\xi \doteq C_0/T^{1/3}$ and

$$\xi \doteq 1 - \frac{C_2 T + C_4 T^2 + C_6 T^3}{1 + C_3 T + C_5 T^2 + C_7 T^3}. \quad (108)$$

The fit coefficients C_i are given by $C_0 = 6.6610 \text{ keV}^{1/3}$, $C_1 = 643.41(10)^{-16} \text{ cm}^3/\text{s}$, $C_2 = 15.136(10)^{-3} \text{ keV}^{-1}$, $C_3 = 65.189(10)^{-3} \text{ keV}^{-1}$, $C_4 = 4.6054(10)^{-3} \text{ keV}^{-2}$, $C_5 = 13.5(10)^{-3} \text{ keV}^{-2}$, $C_6 = -0.10675(10)^{-3} \text{ keV}^{-3}$, and $C_7 = 0.01366(10)^{-3} \text{ keV}^{-3}$. Equation for the reactivity is valid within the $T = [0.2, 100] \text{ keV}$ range and has an error of less than 0.25%. Within the 2–8 keV range, Eq. (107) for the reactivity can be approximated by the following power law:

$$\langle \sigma v \rangle_{\text{DT}} \left(\frac{\text{cm}^3}{\text{s}} \right) \simeq 2.89 \cdot (10)^{-20} [T(\text{keV})]^{3.77}. \quad (109)$$

Using Eq. (109), we then write Eq. (106) in dimensionless form as

$$\frac{dY}{dt} = Y_{\text{ref}} \bar{\rho}^2 \bar{T}^{3.77} \bar{R}_{\text{in}}^2, \quad (110)$$

where the characteristic number for the yield is

$$Y_{\text{ref}} \doteq 1.30 \cdot (10)^{18} [\rho_0 R_{\text{in},0} (\text{g/cm}^2)]^2 \cdot [T(\text{keV})]^{3.77} \cdot [h(\text{cm})] \cdot [t_\varphi(\text{ns})]. \quad (111)$$

This characteristic number will be used in Papers II and III to predict the scaling of the fusion yield.

IX. SUMMARY OF DIMENSIONLESS PARAMETERS CHARACTERIZING A MAGLIF IMPLOSION

Table I summarizes the dimensionless parameters identified in the ODE-based model presented in Secs. II–VIII describing a MagLIF implosion. We now evaluate these parameters to compare their relative importance.

For the circuit model, parameter values describing the Z pulsed-power generator are $Z_0 = 0.18 \Omega$, $L_0 = 9.58 \text{ nH}$, $C = 0.1 \text{ nF}$, and $L_{\text{load}} = 5 \text{ nH}$. For the shunt resistor, typical values are $R_{\text{loss},i} = 80 \text{ Ohm}$, $R_{\text{loss},f} = 0.25 \text{ Ohm}$, $t_{\text{loss}} = 0 \text{ ns}$, and $\Delta t_{\text{loss}} = 5 \text{ ns}$.⁵⁰ As shown in Fig. 2, the characteristic timescale and amplitude of the voltage source are $t_\varphi \simeq 100 \text{ ns}$ and $\varphi_0 \simeq 8.0 \text{ MV}$, respectively. MagLIF liners that are presently studied are $h = 1 \text{ cm}$ long. Upon substituting these values into Eq. (9), we obtain $I_* \simeq 24.5 \text{ MA}$ for the characteristic current, which is close to the typical 20-MA peak current delivered to present-day MagLIF loads.¹⁶ The evaluation of the dimensionless parameters c_1 to c_6 are given in Table I. $c_1 \simeq 0.66$ indicates that the initial total inductance of the system mainly comes from the outer-MITL inductance L_0 . This is understandable since, as the load begins to implode, the inductance grows rapidly, so having $c_1 < 1$ is needed to have good dynamic-inductance matching and power delivery to the load when imploding at peak velocity.⁵¹ The parameter $c_2 \simeq 1.23$ indicates that the voltage drive of the Z circuit is close to resonant with the characteristic $(L_0 + L_1)/Z_0$ time; therefore, the external voltage is driving in an efficient manner the “oscillator” associated to the circuit. The parameter $c_3 \simeq 0.01$ being small denotes that the role of the MITL capacitance in the circuit model in Fig. 1 is minor. This explains why including the MITL capacitance only adds small corrections to the calculation of the current delivered to the loads on the Z machine.³² The parameter $c_4 \simeq 548$ being large means that current transmission is practically lossless in the early times of the current rise. However, $c_5 \simeq 1.71$ means that, at later times in the current pulse, the current transmission is lossy. Finally, the parameter $c_6 \simeq 0.14$ indicates the pulsed-power generator is fairly stiff, and the level of coupling between the imploding load and the pulsed-power generator is relatively small (compared to lower-impedance university-scale generators).

Now, let us consider the dimensionless parameters describing the liner implosion. We consider the typical MagLIF AR=6 liner which has $R_{\text{in},0} = 0.2325 \text{ cm}$, $R_{\text{out},0} = 0.279 \text{ cm}$, and $\hat{m} = 0.138 \text{ g/cm}$. For the characteristic current and the characteristic timescale, we use $I_* \simeq 24.5 \text{ MA}$ and $t_\varphi \simeq 100 \text{ ns}$. The preheat per-unit-length is $\hat{E}_{\text{preheat}} \simeq 2 \text{ kJ/cm}$. The liners are made out of Be. Upon fitting a power law to a cold equation of state²⁷ for Be within the 1000–3000 Mbar range (typical stagnation pressures), we obtain $p_{\text{ref}} \doteq 66.91 \text{ Mbar}$, $\rho_{\text{ref}} \doteq 14 \text{ g/cc}$, and $\gamma \doteq 1.923$. Finally, the initial external magnetic field is $B_{z,0} = 16 \text{ T}$.

Table I shows the evaluation of the dimensionless parameters Π , Φ , Λ , and Σ in Eqs. (37)–(40) when using

TABLE I. Dimensionless parameters characterizing the main physical process occurring in a MagLIF implosion. The plasma conditions used to estimate some of the parameters below are shown in Table II.

Physics model	Parameter	Eq.	Description	Characteristic value (preheat)	Characteristic value (stagnation)
Electrical circuit	c_1	(13)	Ratio of the outer-MITL inductance and total initial inductance of the pulsed-power generator	0.66	
	c_2	(14)	Ratio of characteristic time t_φ of the voltage source and the $(L_0 + L_1)/Z_0$ time constant	1.23	
	c_3	(15)	Ratio of the $\sqrt{(L_0 + L_1)C}$ time constant and the characteristic time t_φ of the voltage source	0.01	
	c_4	(16)	Measure of current transmission to the load region at early stages of the implosion	548	
	c_5	(17)	Measure of current transmission to the load region at later stages of the implosion	1.71	
	c_6	(18)	Coupling parameter between imploding-load inductor and pulsed-power generator	0.14	
Liner implosion	Π	(37)	Ratio of external magnetic potential energy and liner kinetic energy	5.55	
	Φ	(38)	Ratio of fuel internal energy and liner kinetic energy	0.025	
	Λ	(39)	Ratio of liner internal energy and liner kinetic energy	0.614	
	Σ	(40)	Ratio of internal magnetic potential energy and liner kinetic energy	$3.2 \cdot (10)^{-4}$	
Liner stability	Ψ	(50)	Measure of liner robustness towards instabilities	20.4	
Fuel energetics	$\Upsilon_{\alpha,\chi}$	(85)	Ratio of energy source due to α heating and fuel internal energy	-	0.108
	Υ_{rad}	(86)	Ratio of radiation losses and fuel internal energy	0.008	0.384
	Υ_{ce}	(87)	Ratio of electron conduction losses and fuel internal energy	0.007	0.004
	Υ_{ci}	(88)	Ratio of ion conduction losses and fuel internal energy	$2.7 \cdot (10)^{-4}$	0.055
	Υ_{end}	(89)	Ratio of end losses and fuel internal energy. It is also a parameter for mass end losses.	0.103	0.140
Particle transport	$R_{\text{in}}/\ell_\alpha$	(57)	Ratio of plasma-column radius and stopping length of 3.5-MeV α particles	-	0.126
	$R_{\text{in}}/\varrho_\alpha$	(58)	Ratio of plasma-column radius and gyroradius of 3.5-MeV α particles	-	3.70
	x_α	(56)	α -trapping parameter	-	1.42
	η_α	(55)	Fraction of trapped α particles	-	0.68
	x_e	(67)	Electron magnetization	0.60	59.4
	x_i	(68)	Ion magnetization	0.009	0.88
Axial magnetic field transport	Md	(103)	Ratio of magnetic diffusion to rate of flux compression	0.002	0.002
	Ne	(104)	Ratio of Nernst advection to rate of flux compression	0.006	0.004
Fusion yield	Y_{ref}	(111)	Characteristic number for neutron yield	-	$2.04 \cdot (10)^{16}$

these characteristic quantities. $\Pi \simeq 5.55$ is the largest quantity since the magnetic drive is the largest energy source in the problem. Surprisingly though, the second largest quantity is the parameter $\Lambda \simeq 0.614$, which is an order of magnitude larger than the parameter $\Phi \simeq 0.025$ characterizing the fuel internal energy. This indicates that most of the magnetic energy in a MagLIF implosion is directed towards the compression of the liner, not to the fuel. This observation agrees with results from

numerical simulations. For Be liners, the ratio Φ/Λ is

$$\frac{\Phi}{\Lambda} \simeq 0.003 \frac{[\hat{E}_{\text{preheat}}(\text{kJ/cm})]}{[\hat{m}(\text{g/cm})]}. \quad (112)$$

This ratio indicates that, in order to increase partitioning of energy towards the fuel, one must either increase the level of preheat per-unit-length E_{preheat} or reduce the mass of the imploding liner. Regarding the latter option, decreasing the mass of the liners can lead to implosions that are less stable to MRTI. Therefore, there is a trade-off to be made. Current work is underway to develop

TABLE II. Characteristic plasma conditions for the preheat and stagnation phases of a present-day MagLIF implosion.^{10,12,16,20} The preheat temperature is calculated from Eq. (83). Here Δt represents a characteristic timescale of the process considered.

Implosion phase	R_{in} (cm)	h (cm)	ρ (g/cm ³)	T (keV)	B_z (T)	Δt (ns)	$\ln \Lambda$
Preheat	0.2325	1	0.001	0.10	16	10	7
Stagnation	0.01	1	1.0	3.00	10 ⁴	2.5	7

methods to mitigate instabilities, such as the use of coating on the external side of the liner, in order to access liner configurations that are lighter with higher initial aspect ratios. Finally, $\Sigma \simeq 3.2 \cdot (10)^{-4}$ denotes that most of the energy that compressed the MIF core region (fuel and magnetic field) is directed towards compressing the fuel. This actually agrees with the general knowledge that MagLIF plasmas at stagnation generally tend to be high β plasmas, i.e., the magnetic pressure is small compared to the plasma pressure.

Let us now turn our attention to the evaluation of the dimensionless parameters characterizing the fuel energetics. We evaluate these quantities by using the approximate plasma conditions given in Table II for the preheat and stagnation phases of a MagLIF implosion. We consider that the duration of the preheat stage is approximately 10 ns, and the duration of the stagnation stage is 2.5 ns. Assuming that these conditions are also achievable in DT MagLIF experiments, we can evaluate the dimensionless parameters Υ_α , Υ_{rad} , Υ_{ce} , Υ_{ci} , and Υ_{end} .⁵² The results of these calculations are shown in Table I.

During the preheat stage, we note that the main mechanism for energy losses are end losses, followed by radiation loss, and electron-conduction losses. At stagnation, we find that $\Upsilon_\alpha \simeq 0.108$ meaning low α heating for a DT plasma configuration. This is not surprising because the Z facility does not have enough electrical energy and power to reach ignition-relevant conditions. Regarding energy losses, the estimates in Table I show that radiation losses ($\Upsilon_{\text{rad}} \simeq 0.384$) are the most dominant in present-day MagLIF systems. Therefore, when applying similarity scaling to MagLIF loads, one must ensure that the parameter Υ_{rad} is conserved or does not become greater.²⁹ The parameter for ion-conduction losses is $\Upsilon_{\text{ci}} \simeq 0.055$ and is much larger than that for electron-conduction losses. This is not surprising since the high magnetic fields achieved via flux compression are sufficient to highly magnetize the electrons. Finally, evaluation of the end losses shows that $\Upsilon_{\text{end}} \simeq 0.140$, which is larger than Υ_{ci} . Based on these evaluations, we conclude that radiation losses, ion-conduction losses, and end losses are the main energy-loss mechanisms occurring near stagnation of a MagLIF implosion.

Table I also shows the numerical evaluation of other dimensionless parameters characterizing particle-transport, magnetic-field transport, liner stability, and

fusion yield. For the parameters describing the confinement of α particles, we note that the $R_{\text{in}}/\ell_\alpha \gg R_{\text{in}}/\ell_e$ meaning that, if the same conditions were achieved in a MagLIF experiments using DT fuel, most of the confinement of the α particles is due to the flux-compressed magnetic field. According to the parameter η_α , roughly 70% of α particles would be radially confined. Regarding the electron Hall parameter, we observe that electrons are marginally magnetized during the preheat stage and become highly magnetized at stagnation. In contrast, ions are nonmagnetized initially and become marginally magnetized towards the end of the implosion. Since $x_e \gg x_i$, electron thermal conduction is quenched near stagnation, and ion thermal losses dominate. Regarding magnetic-field transport, we highlight that Nernst advection most likely dominates over magnetic diffusion and is approximately uniform throughout the implosion. Finally, substitution of the values given in Table II into Y_{ref} gives a neutron yield of 10x larger than that observed in DT-equivalent yields in present-day MagLIF experiments.¹⁶

X. SIMILARITY SCALING MAGLIF LOADS

A. Definitions and assumptions

Starting with some definitions, we say that two physical systems are *similar* when the characteristics of one of them can be obtained from the characteristics associated with the other by means of a transformation of the input parameters of the problem that leaves the *scale invariants* unchanged. Scale invariants are always dimensionless quantities that are independent of the choice of the system of units. In other words, two phenomena are similar if, and only if, all their dimensionless variables have the same numerical values. With knowledge of the experimental inputs, the stagnation conditions, and performance of a “baseline” MagLIF experiment, we can apply *similarity scaling* to determine the input parameters of scaled MagLIF loads and provide analytical estimates of the stagnation conditions and performance. Likewise, similarity scaling can be helpful to evaluate the veracity of MagLIF design simulations by comparing results corresponding to sets of carefully similarity-scaled MagLIF load designs.

To apply similarity scaling to MagLIF, we make the following first assumption:

1. We assume that the reduced models introduced in Secs. II–VIII capture the main physical mechanisms at play in an imploding MagLIF load and are sufficient to qualitatively describe the *trends* in performance metrics when varying the experimental parameters.

Of course, additional physical processes are missing: for example, skin effects in the current-driven liner, the finite time it takes α particles to slow down, and radiation emission by mix. We assume that the processes described

in Secs. II–VIII determine to leading order the dynamics of MagLIF implosions and that other missing physical processes provide next-order corrections. Our assumption #1 seems reasonable because the model proposed in this paper is a simplified version of the more sophisticated analytical model in Ref. 27, which has been shown to sufficiently reproduce prediction trends of the more complex, multiphysics-code simulations (see Ref. 28).

One important consequence of Assumption #1 is that any dimensionless quantity can be written as a relationship between scale invariants, i.e., the identified dimensionless parameters. More specifically, by inspection of the dimensionless equations presented in this paper, any dimensionless quantity \bar{Q} can be determined by

$$\bar{Q} = F_{\bar{\varphi}_{oc},f}(c_{1-6}, \bar{t}_i, \Pi, \Phi, \Lambda, \Sigma, \Psi, \Upsilon_\alpha, \Upsilon_{rad}, \Upsilon_{ce}, \Upsilon_{ci}, \dots, R_{in}/\ell_\alpha, R_{in}/\varrho_\alpha, x_\alpha, \eta_\alpha, x_e, x_i, \text{Md}, \text{Ne}), \quad (113)$$

where the function $F_{\bar{\varphi}_{oc},f}$ depends on the dimensionless time trace $\bar{\varphi}_{oc}$ of the voltage drive and on the function f parameterizing the behavior of the shunt resistor R_{loss} . (\bar{t}_i denotes the dimensionless time parameters corresponding to t_{loss} , Δt_{loss} and $t_{preheat}$.) As an example of how Eq. (113) can be used, the dimensionless fuel pressure at stagnation is $\bar{p}_{fuel,stag} \doteq \bar{p}_{fuel}(\bar{t} = \bar{t}_{stag})$. From the equation above and using Eq. (28), the physical fuel pressure $p_{fuel,stag}$ at stagnation will be given by

$$\bar{p}_{stag} = \frac{p_{fuel,stag}}{p_{preheat}} = F_{\bar{\varphi}_{oc},f}(c_{1-6}, \bar{t}_i, \dots, \text{Md}, \text{Ne}). \quad (114)$$

Therefore, we have a relationship between the fuel pressure at stagnation, the pressure achieved during preheat [defined in Eq. (29)], and the function $F_{\bar{\varphi}_{oc},f}$ of the scale invariants. Note that $p_{preheat}$ is function of the experimental input parameters so it is known *a priori*.

We state our second assumption as follows:

2. No- α quantities, i.e., quantities obtained in the absence of α heating, can be used as good surrogates for performance metrics of MagLIF configurations.

For present-day MagLIF configurations fielded on the Z facility, the attained stagnation conditions are not sufficient for robust α heating. Therefore, α -heating can be neglected. However, significant α heating and high yields could be achieved on a future larger pulsed-power driver.^{8,11,27,53,54} For such higher-current scenarios, we shall use similarity scaling to estimate the stagnation conditions that are achievable in the absence of α heating and evaluate how promising they are to lead towards robust α -heating scenarios. Studying the scaling of no- α quantities was proposed in Ref. 39 for laser-direct-drive ICF implosions.

We shall use the subscript “no α ” to denote quantities in the absence of α heating. The functional relationship for “no α ” quantities is obtained by removing the dimen-

sionless parameters related to α heating in Eq. (113):

$$\bar{Q}_{no\alpha} = \mathcal{F}_{\bar{\varphi}_{oc},f}(c_{1-6}, \bar{t}_i, \Pi, \Phi, \Lambda, \Sigma, \Psi, \Upsilon_{rad}, \Upsilon_{ce}, \dots, \Upsilon_{ci}, \Upsilon_{end}, x_e, x_i, \text{Md}, \text{Ne}), \quad (115)$$

where $\mathcal{F}_{\bar{\varphi}_{oc},f}$ denotes the function $F_{\bar{\varphi}_{oc},f,no\alpha}$.

Our third and final assumption is the following.

3. Among the dimensionless “no α ” parameters, the parameters that determine to leading order the dynamics and performance of a MagLIF implosion are: (i) the parameters (c_{1-6}) determining the circuit-load coupling, (ii) the Π parameter determining the liner implosion, (iii) the Φ parameter characterizing the preheat, (iv) the parameter Ψ measuring robustness towards hydrodynamic instabilities, and (v) the parameters ($\Upsilon_{rad}, \Upsilon_{ci}, \Upsilon_{end}$) characterizing the radiation, ion-conduction, and end loss mechanisms.

It can be easily shown that, with the available experimental input parameters defining a MagLIF load, it is not possible to conserve all the dimensionless quantities on the right-hand side of Eq. (115). (Basically, the number of constraints to satisfy is larger than the number of independent experimental input parameters.) To overcome this difficulty, we introduce the notion of *essential dimensionless variables*. A dimensionless parameter \bar{Q} is considered essential when its value is neither too small or too large, e.g. if its value lies within the range 0.1–10. If the dimensionless parameter \bar{Q} lies outside this range, it is assumed that its influence in the phenomenon is negligible, and it is therefore considered a *non-essential dimensionless variable*.⁵⁵ One example of a non-essential parameter is Σ , which measures the ratio of the axial magnetic energy within the fuel and the characteristic kinetic energy of the liner. According to Table I, Σ is a small number for typical MagLIF implosions. Therefore, conserving such parameter is not needed. Likewise, the parameters describing magnetic transport (Md and Ne) are also small, and the electron Hall parameter x_e near stagnation is large. We can consider these dimensionless variables to be non-essential. As shown in Table I, ion-conduction losses dominate over electron-conduction losses at stagnation. Since Υ_{ce} and Υ_{ci} are the sole energy-confinement parameters that depend on the applied magnetic field, we must then choose the scaling of $B_{z,0}$ so that Υ_{ci} remains invariant.

Although numerical evaluation of dimensionless parameters is a powerful tool to determine which dimensionless parameters are more essential than others, this procedure is sometimes insufficient. In some cases, a MagLIF designer or experimentalist must tap into his/her physical intuition and decide which parameters are the most relevant to conserve when studying a physical mechanism at play. When only a subset of the scale invariants appearing in a problem can be conserved simultaneously, we then have an *incomplete similarity scaling*. When incomplete similarity scaling conserves essential scale invariants, there is a good chance that the

scaling rules and subsequent scaling extrapolations will lead to predictable outcomes. For MagLIF implosions, the conserved dimensionless parameters mentioned in Assumption #3 are those that (we assume) govern the main ingredients characterizing a MagLIF implosion: power delivery to the load, implosion and compression of the fusion fuel, and energy confinement of the assembled hot fuel. Assumption #3 will nevertheless need to be verified via numerical simulations of MagLIF loads and by experiments dedicated to studying scaling physics.

One mathematical consequence of Assumption #3 is that the functional relation between dimensionless quantities can be simplified to

$$\bar{Q}_{\text{no } \alpha} \simeq \mathcal{F}_{\bar{\varphi}_{\text{oc}}, f}^{(0)}(c_{1-6}, \bar{t}_i, \Pi, \Phi, \Psi, \Upsilon_{\text{rad}}, \Upsilon_{\text{ce}}, \Upsilon_{\text{ci}}, \Upsilon_{\text{end}}), \quad (116)$$

where we have replaced $\mathcal{F}_{\bar{\varphi}_{\text{oc}}, f}$ by the function $\mathcal{F}_{\bar{\varphi}_{\text{oc}}, f}^{(0)}$ which no longer has the parameters Λ , Σ , Υ_{ce} , x_e , x_i , Md, and Ne in its arguments.

There are several physical consequences of the approximation above. Since the parameters Λ and Σ no longer appear, this implies that the internal energy of the liner and the potential energy of the flux-compressed magnetic field within the fuel are not important for determining conditions within the fuel. Regarding the latter, this is a good approximation since MagLIF plasmas are high- β plasmas. Regarding the former, this is a much stronger and questionable approximation since the evaluation of the parameter Λ in Table I shows that it is not a negligible quantity. Therefore, dropping Λ in Eq. (116) is not entirely warranted; this approximation will have to be verified *a posteriori* in the scaling studies in Papers II and III. In a related manner, since the quantities Md and Ne no longer appear in Eq. (116), effects from magnetic diffusion and Nernst advection are ignored in the similarity scaling.

After having mentioned our three assumptions, we are now in the position to discuss how similarity scaling will be used to explore the parameter space of MagLIF implosions. Starting from the example given above, suppose that we are interested in determining the stagnation pressure of a scaled MagLIF load. Based on the arguments above, the functional relationship for the stagnation pressure is approximately written as

$$\frac{p_{\text{stag, no } \alpha}}{p_{\text{preheat}}} \simeq \mathcal{F}_{\bar{\varphi}_{\text{oc}}, f}^{(0)}(c_{1-6}, \bar{t}_i, \Pi, \Phi, \Psi, \Upsilon_{\text{rad}}, \Upsilon_{\text{ce}}, \Upsilon_{\text{ci}}, \Upsilon_{\text{end}}). \quad (117)$$

As shown in Sec. XB, the input parameters of the circuit and of a MagLIF load can be scaled so that the dimensionless quantities appearing on the right-hand side of Eq. (117) are all conserved. Therefore, the right-hand side of Eq. (117) can be considered a constant so that

$$p_{\text{stag, no } \alpha} \simeq \frac{E_{\text{preheat}}}{R_{\text{in}, 0}^2 h} \times \text{const.}, \quad (118)$$

where we used Eq. (29). This relationship holds true for any family of similarity-scaled MagLIF loads

that are characterized by the same scale invariants (c_{1-6} , \bar{t}_i , Π , Φ , Ψ , Υ_{rad} , Υ_{ce} , Υ_{ci} , Υ_{end}). Suppose that the stagnation pressure $p_{\text{stag, no } \alpha}$ is known for a “baseline” MagLIF configuration. If a scaled MagLIF configuration has the same scale invariants, then its stagnation pressure $p'_{\text{stag, no } \alpha}$ will be given by

$$p'_{\text{stag, no } \alpha} = p_{\text{stag, no } \alpha} \left(\frac{E'_{\text{preheat}}}{E_{\text{preheat}}} \right) \left(\frac{R_{\text{in}, 0}^2 h}{R_{\text{in}, 0}'^2 h'} \right), \quad (119)$$

where the quantities with apostrophes correspond to those of the scaled configuration. In other words, by leveraging similarity scaling, we can estimate the solutions corresponding to a second set of input parameters by first taking the known baseline solution and multiplying it by a known function of the two sets of input parameters for different similarity-scaled configurations. In other words, similarity scaling allows the projection of known solutions in a parameter space that has been explored to a new parameter space as long as the scale invariants describing the system remain unchanged. In this example, we have taken the specific case of the stagnation pressure, but similar arguments hold for other experimental quantities of interest: for example, peak current, bang time, fuel temperature at peak burn, energy within the liner and the fuel, magnetic flux at stagnation, burn-width time, and neutron yield. Applying similarity scaling therefore allows to reduce risks when doing extrapolations in performance by constraining the scaled loads to remain in a similar operating regime that is well understood experimentally or in numerical simulations.

B. General similarity-scaling prescriptions

Let us now derive the scaling relations for the experimental input parameters characterizing the electrical circuit and a MagLIF load. When enforcing conservation of the dimensionless circuit parameters describing the circuit model [see Eqs. (13)–(18)], we find

$$c_1: \quad \frac{L'_1}{L_1} = \frac{L'_0}{L_0} = \frac{h'}{h}, \quad (120)$$

$$c_2: \quad \frac{Z'_0}{Z_0} = \frac{L'_0 t_\varphi}{L_0 t'_\varphi} = \frac{h' t_\varphi}{h t'_\varphi}, \quad (121)$$

$$c_3: \quad \frac{C'}{C} = \frac{L_0}{L'_0} \left(\frac{t'_\varphi}{t_\varphi} \right)^2 = \frac{h}{h'} \left(\frac{t'_\varphi}{t_\varphi} \right)^2, \quad (122)$$

$$c_4: \quad \frac{R'_{\text{loss}, i}}{R_{\text{loss}, i}} = \frac{L'_0 t_\varphi}{L_0 t'_\varphi} = \frac{h' t_\varphi}{h t'_\varphi}, \quad (123)$$

$$c_5: \quad \frac{R'_{\text{loss}, f}}{R_{\text{loss}, f}} = \frac{L'_0 t_\varphi}{L_0 t'_\varphi} = \frac{h' t_\varphi}{h t'_\varphi}, \quad (124)$$

$$c_6: \quad \frac{L'_0}{L_0} = \frac{h'}{h}. \quad (125)$$

All temporal variables should scale with the voltage characteristic time. Therefore, the time parameters describ-

ing the shunt resistor are scaled as

$$\bar{t}_i: \quad \frac{t'_{\text{loss}}}{t_{\text{loss}}} = \frac{t'_\varphi}{t_\varphi}, \quad \frac{\Delta t'_{\text{loss}}}{\Delta t_{\text{loss}}} = \frac{t'_\varphi}{t_\varphi}. \quad (126)$$

As a reminder, for an arbitrary quantity Q corresponding to the *baseline* set of input parameters, the quantity Q' denotes its *scaled* value for the second set of input parameters.

The origin of the scaling prescriptions in Eqs. (120)–(125) can be understood from the effects that the parameters c_1 to c_6 measure. As an example, in Papers II and III, we investigate similarity scaling of MagLIF loads when the peak current and characteristic timescale t_φ of the external voltage source are varied. As shown in those papers, the target height changes when scaling according to these parameters. To maintain the relative impedance of the electrical circuit when imploding shorter or longer targets, the dimensionless quantity c_6 constrains that the circuit inductance L_0 scale with the target height. The rest of the scaling prescriptions in Eqs. (120)–(126) follow from similar arguments.

In scaling studies of MIF concepts to larger and more energetic pulsed-power drivers, the extrapolation is usually done in terms of the peak current delivered to the load (e.g., see Refs. 56 and 57). However, peak current delivered to the load is a result from the solution of the electrical circuit equations, and therefore, does not suit well as an independent variable for similarity scaling. Luckily, the characteristic current I_\star in Eq. (9) can serve as such variable. Noting that $I_\star = (\varphi_0 t_\varphi / L_0)[c_1/(1+c_2)]$ and using conservation of the parameters c_1 and c_2 , we find the scaling prescription for the characteristic voltage φ_0 :

$$\frac{\varphi'_0}{\varphi_0} = \frac{I'_\star t_\varphi L'_0}{I_\star t'_\varphi L_0} = \frac{I'_\star t_\varphi h'}{I_\star t'_\varphi h}. \quad (127)$$

All measured voltages in the circuit model of Fig. 1 will scale according to the prescription above. As expected, the voltage φ_0 increases when the characteristic current increases. It also increases when the characteristic time t_φ decreases because of the larger inductive voltage. Finally, when driving shorter or longer liners, the voltage φ_0 will also scale proportionally to h .

Among the dimensionless parameters describing the liner dynamics, the most important quantity to conserve is the Π parameter, which characterizes the magnetic drive of the implosion. We also wish to conserve the robustness of the MagLIF liner towards MRTI when scaling the input parameters. Thus, we have $\Pi = \text{const}$ and $\Psi = \text{const}$. When combining these two constraints, we find that the liner outer radius and the liner mass per-unit-length must scale as follows:

$$\Pi \ \& \ \Psi: \quad \frac{R'_{\text{out},0}}{R_{\text{out},0}} = \left[\left(\frac{I'_\star}{I_\star} \right)^{1-1/\gamma} \left(\frac{t'_\varphi}{t_\varphi} \right) \right]^{\frac{1}{2-1/\gamma}}, \quad (128)$$

$$\Pi \ \& \ \Psi: \quad \frac{\hat{m}'}{\hat{m}} = \left[\left(\frac{I'_\star}{I_\star} \right)^2 \left(\frac{t'_\varphi}{t_\varphi} \right)^{2-2/\gamma} \right]^{\frac{1}{2-1/\gamma}}. \quad (129)$$

Following these scaling rules guarantees that the liner will implode in a similar fashion and that its robustness towards instabilities will be maintained. For the sake of completeness, the liner inner radius will then follow

$$R'_{\text{in},0} = [R'^2_{\text{out},0} - \hat{m}'/(\pi \rho_{\text{liner},0})]^{1/2}. \quad (130)$$

By conservation of the parameter Φ in Eq. (38), which determines the pushback of the fuel pressure on the imploding liner, we find that the scaling relation for the preheat energy per-unit-length is given by

$$\Phi: \quad \frac{\hat{E}'_{\text{preheat}}}{\hat{E}_{\text{preheat}}} = \left(\frac{I'_\star}{I_\star} \right)^2. \quad (131)$$

This relation can be found by dividing the two constant parameters Π and Φ . We therefore find that the preheat energy per-unit-length scales as the characteristic current squared. Since all time parameters scale with the characteristic timescale of the voltage drive, then the preheat timing will also scale accordingly:

$$\bar{t}_i: \quad \frac{t'_{\text{preheat}}}{t_{\text{preheat}}} = \frac{t'_\varphi}{t_\varphi}. \quad (132)$$

Physically, this scaling law ensures that preheat will occur at the same moment of the implosion (in terms of the inner convergence ratio CR_{in}).

We still need to determine the scaling prescriptions for the initial fuel density ρ_0 , the applied external magnetic field $B_{z,0}$, and the liner height h . From the discussion in Sec. X A, the scaling prescriptions for these input parameters are determined by fixing the dimensionless parameters describing relative radiation losses, ion-conduction losses, and end losses. Before proceeding, we note that the dimensionless parameter for ion-conduction losses behaves as $\Upsilon_{\text{ci}} \propto T_{\text{preheat}} t_\varphi / (B_0 R_{\text{in},0}^2)$ in the marginal-magnetization regime for ions, which is an appropriate assumption near stagnation. We then obtain the following scaling rules:

$$\Upsilon_{\text{rad}}: \quad \frac{\rho'_0}{\rho_0} = \left(\frac{I'_\star}{I_\star} \right)^{2/3} \left(\frac{R'_{\text{in},0}}{R_{\text{in},0}} \right)^{-2/3} \left(\frac{t'_\varphi}{t_\varphi} \right)^{-2/3}, \quad (133)$$

$$\Upsilon_{\text{ci}}: \quad \frac{B'_{z,0}}{B_{z,0}} = \left(\frac{I'_\star}{I_\star} \right)^{4/3} \left(\frac{R'_{\text{in},0}}{R_{\text{in},0}} \right)^{-10/3} \left(\frac{t'_\varphi}{t_\varphi} \right)^{5/3}, \quad (134)$$

$$\Upsilon_{\text{end}}: \quad \frac{h'}{h} = \left(\frac{I'_\star}{I_\star} \right)^{2/3} \left(\frac{R'_{\text{in},0}}{R_{\text{in},0}} \right)^{-2/3} \left(\frac{t'_\varphi}{t_\varphi} \right)^{4/3}. \quad (135)$$

To obtain these scaling prescriptions, we have used Eq. (83) to eliminate the preheat temperature T_{preheat} in favor of the preheat energy per-unit-length \hat{E}_{preheat} . We then substituted Eq. (131). Finally, the scaling of the preheat energy delivered to the MagLIF fuel volume is given by

$$\frac{E'_{\text{preheat}}}{E_{\text{preheat}}} = \frac{\hat{E}'_{\text{preheat}}}{\hat{E}_{\text{preheat}}} \frac{h'}{h}. \quad (136)$$

In summary, Eqs. (120)–(136) are the scaling prescriptions for MagLIF experimental input parameters when varying the characteristic current (or equivalently, the peak current) delivered to the load and when varying the characteristic time of the voltage drive (or equivalently, the rise time of the current trace). In Papers II and III, we shall use these scaling prescriptions and test similarity scaling according to I_* and t_φ via numerical simulations.

XI. CONCLUSIONS

Pulsed-power driven MagLIF loads are complex systems that involve multiple processes that govern the electrical-circuit dynamics, liner-implosion dynamics, hydrodynamic instabilities, fuel-energy losses, particle transport, fuel-mass losses, axial magnetic-field transport, fusion yield, etc. Moreover, the experimental input parameters defining a MagLIF load are numerous. Given the complexity of MagLIF implosions and the relatively high dimensionality of the input-parameter space, detailed explorations of MagLIF performance is computationally expensive using radiation-hydrodynamic simulations and virtually impossible via integrated experiments on Z. However, surveys of MagLIF performance in the input-parameter space can be simplified via the use of *dimensional analysis* and *similarity scaling*.

In Paper I of this series, we presented a theoretical framework for similarity scaling MagLIF loads. We developed a simplified analytical model based on ordinary differential equations (ODEs) that describes the main mechanisms at play occurring during a MagLIF implosion. After introducing the governing equations, we performed a dimensional analysis to determine the most important dimensionless parameters characterizing MagLIF implosions. We also provided estimates of such parameters using typical fielded or experimentally observed stagnation quantities for MagLIF. We then showed that MagLIF loads can be *incompletely similarity scaled*, meaning that the experimental input parameters of MagLIF can be varied such that many (but not all) of the dimensionless quantities characterizing a MagLIF implosion are conserved. Following arguments based on similarity scaling, we can then estimate the performance of similarity scaled MagLIF loads when using this framework.

Specific applications of these results are left to Refs. 30 and 31 (also referred as Papers II and III of this series). In Paper II, we address the problem of scaling MagLIF targets with respect to electrical current delivered to the load. In Paper III, we study the scaling MagLIF loads when the characteristic timescale of the voltage drive (or equivalently, the current rise-time) is varied.

The present work can be extended in several directions. First, there are “hidden” dimensionless variables that are not captured in the present model. Examples of known physical processes that are not discussed are: (i) magnetic diffusion of the external magnetic field

into the liner, (ii) magnetic-field advection due to Hall physics related to the tenuous plasmas surrounding the MagLIF liner, (iii) the role of the helical structures observed in MagLIF-like implosions,^{58,59} (iv) the electro-thermal instability,^{60–64} (v) the introduction of mix from the liner to the hot fuel,¹³ and (vi) degradation of α -particle confinement due to liner instabilities. Understanding how these processes affect MagLIF performance and how they scale remains an important task. Second, future scaling studies can be more focused towards the physics of the laser-preheat process itself. In Ref. 29, a preliminary scaling analysis was presented on the estimated stopping length of the laser and laser–plasma interactions. This analysis could be further improved and corroborated against numerical simulations, as well as dedicated experiments.⁶⁵ Finally, dimensional analysis and similarity scaling may be useful for understanding the physics behind the pulsed-power delivery to a MagLIF load. This effort would involve developing a suitable analytical model for describing current losses in the magnetically-insulated transmission lines. Such a study could then provide guidance on risks associated to pulsed-power delivery when extrapolating to higher current densities in a future pulsed-power machine.

One of the authors (D. E. Ruiz) was supported in part by Sandia National Laboratories (SNL) Laboratory Directed Research and Development (LDRD) Program, Project 223312. Sandia National Laboratories is a multi-mission laboratory managed and operated by National Technology & Engineering Solutions of Sandia, LLC, a wholly owned subsidiary of Honeywell International Inc., for the U.S. Department of Energy’s National Nuclear Security Administration under contract DE-NA0003525. This paper describes objective technical results and analysis. Any subjective views or opinions that might be expressed in the paper do not necessarily represent the views of the U.S. Department of Energy or the United States Government.

Appendix A: Rarefaction wave

We model the flow outflow from the openings of the imploding liner as a rarefaction wave. The 1D Euler equations are

$$\partial_t \rho + u \partial_x \rho = -\rho \partial_x u, \quad (\text{A1})$$

$$\rho \partial_t u + \rho u \partial_x u = -\partial_x p, \quad (\text{A2})$$

$$\partial_t S + u \partial_x S = 0, \quad (\text{A3})$$

where ρ , u , p , and S are the fluid density, velocity, pressure, and entropy, respectively. Following Ref. 66, we propose self-similar solutions of the form $f = f(\xi)$, where $\xi \doteq x/t$. In terms of ξ , the 1D Euler equations for isen-

tropic flow are

$$(u - \xi) \frac{d\rho}{d\xi} = -\rho \frac{du}{d\xi}, \quad (\text{A4})$$

$$\rho(u - \xi) \frac{du}{d\xi} = -\frac{dp}{d\xi}, \quad (\text{A5})$$

$$(u - \xi) \frac{dS}{d\xi} = 0. \quad (\text{A6})$$

The last equation implies that $dS/d\xi = 0$. Combining the first and second equations, we obtain

$$(u - \xi)^2 \frac{d\rho}{d\xi} = \frac{dp}{d\xi} = \left(\frac{dp}{d\rho} \right)_S \frac{d\rho}{d\xi} = c^2 \frac{d\rho}{d\xi}. \quad (\text{A7})$$

Because the flow is isentropic, the pressure p is only dependent on the fluid density: $p = p(\rho)$, and the local sound speed is denoted by $c \doteq (\partial p / \partial \rho)_S^{1/2}$. A nontrivial solution for Eq. (A7) is given by

$$u - \xi = \pm c. \quad (\text{A8})$$

Substituting this result into Eqs. (A4) and (A5) gives

$$du \pm c \frac{d\rho}{\rho} = du \pm \frac{dp}{\rho c} = 0. \quad (\text{A9})$$

Therefore, the following two functions are constants:

$$J_{\pm} \doteq u \pm \int \frac{dp}{\rho c} = u \pm \int c \frac{d\rho}{\rho} = \text{const}. \quad (\text{A10})$$

For an ideal gas, the integral quantities $\int dp/(\rho c) = \int c d\rho/\rho$, can be expressed in terms of the local speed of sound c alone. For example, for a perfect gas with constant specific heats and $\gamma = 5/3$, we have

$$p = p_0 \left(\frac{\rho}{\rho_0} \right)^{5/3}, \quad (\text{A11})$$

$$c^2 = \frac{\partial p}{\partial \rho} = c_0^2 \left(\frac{\rho}{\rho_0} \right)^{2/3}, \quad (\text{A12})$$

where $c_0^2 \doteq \gamma p_0 / \rho_0$ and u_0 is the reference internal energy of the gas. Hence, the invariants (A10) are written as

$$J_{\pm} = u \pm 3c = \text{const}. \quad (\text{A13})$$

To determine the constant, let us assume a rarefaction wave propagating towards a gas whose density, pressure, and sound speed (ρ_0, p_0, c_0) initially occupy the half space $x > 0$. At the edge of the propagating rarefaction wave, the fluid has not begun to move so $u = 0$. Hence,

$$J_- = u - 3c = -3c_0. \quad (\text{A14})$$

(The negative sign is chosen so that $u < 0$, which means that the rarefaction wave expands towards the left.) We can then write the local sound speed c as a function of the local fluid velocity u :

$$c = c_0 - u/3. \quad (\text{A15})$$

Using the thermodynamic relations (A12), we can also write the fluid density and pressure as functions of u :

$$\rho = \rho_0 \left(1 + \frac{u}{3c_0} \right)^3, \quad p = p_0 \left(1 + \frac{u}{3c_0} \right)^5. \quad (\text{A16})$$

The fluid expands towards the vacuum region ($x < 0$). At the left boundary of the rarefaction wave, the fluid density and pressure are zero. Hence, the edge of the rarefaction wave will travel at three times the speed of sound of the unperturbed fluid

$$|u|_{\text{max}} = 3c_0. \quad (\text{A17})$$

When combining Eqs. (A8) and (A15), we obtain

$$u = \frac{3}{4}(\xi - c_0) = \frac{3}{4}c_0 \left(\frac{x}{c_0 t} - 1 \right). \quad (\text{A18})$$

The left boundary of the rarefaction wave facing the vacuum travels at a velocity $u = -3c_0$, so from the equation above, the left front of the rarefaction wave is given by $x = -3c_0 t$. At the right boundary of the rarefaction wave facing the fluid, one has $u = 0$. Therefore, the right front of the rarefaction wave is given by $x = c_0 t$.

Let us now calculate the mass fuel losses through the axial openings of a MagLIF liner. The fuel mass lost $m_L(t)$ is defined as the total fluid mass that has passed the $x = 0$ plane at a given time t . This leads to

$$\begin{aligned} m_L(t) &\doteq 2\pi R_c^2 \int_{-3c_0 t}^0 \rho(t, x) dx \\ &= 2\pi R_c^2 \rho_0 \int_{-3c_0 t}^0 \left[1 + \frac{1}{4} \left(\frac{x}{c_0 t} - 1 \right) \right]^3 dx \\ &= 2 \left(\frac{3}{4} \right)^4 \rho_0 (\pi R_c^2) t c_0, \\ &\simeq 0.63 \rho_0 (\pi R_c^2) t c_0. \end{aligned} \quad (\text{A19})$$

In the equation above, the factor 2 accounts for the fact that the fuel can escape through the top and bottom ends of the liner. In the second line, we substituted Eqs. (A16) and (A18). We also introduced the transverse area πR_c^2 through which the fluid escapes. We assume that the change of the transverse area and of the background fluid density and sound speed are slow compared to the propagation of the rarefaction wave into the fuel. Thus, the resulting equation for the total fuel mass within the fuel cavity of a MagLIF liner is given by

$$\frac{dm}{dt} = -0.63 \pi \rho_0(t) c_0(t) R_c^2(t), \quad (\text{A20})$$

Substituting $m = \pi R_{\text{in}}^2 \rho$ into Eq. (A20) leads to Eq. (90).

To estimate the corresponding energy losses due to the fuel outflow, we define $\epsilon_L(t)$ as the difference between the initial internal energy and the internal energy at time t contained in the region $0 \leq x \leq c_0 t$, i.e., where the rarefaction wave has perturbed the background fluid at

rest. For an ideal gas with $\gamma = 5/3$, the internal energy per-unit-volume is $(3/2)p$. Hence,

$$U_L(t) \doteq 2 \left(\frac{3}{2} \right) \pi R_c^2 \int_0^{c_0 t} [p_0 - p(t, x)] dx$$

Upon substituting Eq. (A16) and integrating, we find

$$\begin{aligned} U_L(t) &= \left(\frac{3}{2} \right) \left[\frac{2}{3} + \left(\frac{3}{4} \right)^5 \right] p_0 (\pi R_c^2) t c_0, \\ &\simeq 0.90 \hat{U}_0 \frac{R_c^2}{R_{in}^2} t c_0, \end{aligned} \quad (\text{A21})$$

where we introduced the internal energy per-unit-length in the fuel such that $\hat{U}_0 \doteq (3/2)p_0(\pi R_{in}^2)$. Taking the leading-order time derivative leads to Eq. (71).

- ¹J. D. Lindl, P. Amendt, R. L. Berger, S. G. Glendinning, S. H. Glenzer, S. W. Haan, R. L. Kauffman, O. L. Landen, and L. J. Suter, “The physics basis for ignition using indirect-drive targets on the National Ignition Facility,” *Phys. Plasmas* **11**, 339 (2004).
- ²O. A. Hurricane, P. T. Springer, P. K. Patel, D. A. Callahan, K. Baker, D. T. Casey, L. Divol, T. Döppner, D. E. Hinkel, M. Hohenberger, et al., “Approaching a burning plasma on the NIF,” *Phys. Plasmas* **26**, 052704 (2019).
- ³H. Abu-Shawareb, R. Acree, P. Adams, J. Adams, B. Addis, R. Aden, P. Adrian, B. B. Afeyan, M. Aggleton, L. Aghaian, et al. (Indirect Drive ICF Collaboration), “Lawson criterion for ignition exceeded in an inertial fusion experiment,” *Phys. Rev. Lett.* **129**, 075001 (2022).
- ⁴A. B. Zylstra, A. L. Kritcher, O. A. Hurricane, D. A. Callahan, J. E. Ralph, D. T. Casey, A. Pak, O. L. Landen, B. Bachmann, K. L. Baker, et al., “Experimental achievement and signatures of ignition at the national ignition facility,” *Phys. Rev. E* **106**, 025202 (2022).
- ⁵A. L. Kritcher, A. B. Zylstra, D. A. Callahan, O. A. Hurricane, C. R. Weber, D. S. Clark, C. V. Young, J. E. Ralph, D. T. Casey, A. Pak, et al., “Design of an inertial fusion experiment exceeding the lawson criterion for ignition,” *Phys. Rev. E* **106**, 025201 (2022).
- ⁶I. R. Lindemuth and R. C. Kirkpatrick, “Parameter space for magnetized fuel targets in inertial confinement fusion,” *Nucl. Fusion* **23**, 263 (1983).
- ⁷I. R. Lindemuth, “The ignition design space of magnetized target fusion,” *Phys. Plasmas* **22**, 122712 (2015).
- ⁸S. A. Slutz, W. A. Stygar, M. R. Gomez, K. J. Peterson, A. B. Sefkow, D. B. Sinars, R. A. Vesey, E. M. Campbell, and R. Betti, “Scaling magnetized liner inertial fusion on Z and future pulsed-power accelerators,” *Phys. Plasmas* **23**, 022702 (2016).
- ⁹S. A. Slutz, M. C. Herrmann, R. A. Vesey, A. B. Sefkow, D. B. Sinars, D. C. Rovang, K. J. Peterson, and M. E. Cuneo, “Pulsed-power-driven cylindrical liner implosions of laser preheated fuel magnetized with an axial field,” *Phys. Plasmas* **17**, 056303 (2010).
- ¹⁰M. R. Gomez, S. A. Slutz, A. B. Sefkow, D. B. Sinars, K. D. Hahn, S. B. Hansen, E. C. Harding, P. F. Knapp, P. F. Schmit, C. A. Jennings, et al., “Experimental demonstration of fusion-relevant conditions in magnetized liner inertial fusion,” *Phys. Rev. Lett.* **113**, 155003 (2014).
- ¹¹A. B. Sefkow, S. A. Slutz, J. M. Koning, M. M. Marinak, K. J. Peterson, D. B. Sinars, and R. A. Vesey, “Design of magnetized liner inertial fusion experiments using the Z facility,” *Phys. Plasmas* **21**, 072711 (2014).
- ¹²M. R. Gomez, S. A. Slutz, P. F. Knapp, K. D. Hahn, M. R. Weis, E. C. Harding, M. Geissel, J. R. Fein, M. E. Glinsky, S. B. Hansen, et al., “Assessing Stagnation Conditions and Identifying Trends in Magnetized Liner Inertial Fusion,” *IEEE Trans. Plasma Sci.* **47**, 2081 (2019).
- ¹³P. F. Knapp, M. R. Gomez, S. B. Hansen, M. E. Glinsky, C. A. Jennings, S. A. Slutz, E. C. Harding, K. D. Hahn, M. R. Weis, M. Evans, et al., “Origins and effects of mix on magnetized liner inertial fusion target performance,” *Phys. Plasmas* **26**, 012704 (2019).
- ¹⁴D. B. Sinars, M. A. Sweeney, C. S. Alexander, D. J. Ampleford, T. Ao, J. P. Apruzese, C. Aragon, D. J. Armstrong, K. N. Austin, T. J. Awe, et al., “Review of pulsed power-driven high energy density physics research on Z at Sandia,” *Phys. Plasmas* **27**, 070501 (2020).
- ¹⁵D. A. Yager-Elorriaga, M. R. Gomez, D. E. Ruiz, S. A. Slutz, A. J. Harvey-Thompson, C. A. Jennings, P. F. Knapp, P. F. Schmit, M. R. Weis, T. J. Awe, et al., “An overview of magneto-inertial fusion on the Z machine at Sandia National Laboratories,” *Nucl. Fusion* **62**, 042015 (2022).
- ¹⁶M. R. Gomez, S. A. Slutz, C. A. Jennings, D. J. Ampleford, M. R. Weis, C. E. Myers, D. A. Yager-Elorriaga, K. D. Hahn, S. B. Hansen, E. C. Harding, et al., “Performance scaling in magnetized liner inertial fusion experiments,” *Phys. Rev. Lett.* **125**, 155002 (2020).
- ¹⁷M. R. Weis, A. J. Harvey-Thompson, and D. E. Ruiz, “Scaling laser preheat for MagLIF with the Z-Beamlet laser,” *Phys. Plasmas* **28**, 012705 (2021).
- ¹⁸A. J. Harvey-Thompson, M. R. Weis, D. E. Ruiz, M. S. Wei, A. B. Sefkow, T. Nagayama, E. M. Campbell, J. A. Fooks, M. E. Glinsky, and K. J. Peterson, “The effect of laser entrance hole foil thickness on MagLIF-relevant laser preheat,” *Phys. Plasmas* **27**, 113301 (2020).
- ¹⁹A. J. Harvey-Thompson, M. Geissel, C. A. Jennings, M. R. Weis, M. R. Gomez, J. R. Fein, D. J. Ampleford, G. A. Chandler, M. E. Glinsky, K. D. Hahn, et al., “Constraining preheat energy deposition in MagLIF experiments with multi-frame shadowgraphy,” *Phys. Plasmas* **26**, 032707 (2019).
- ²⁰A. J. Harvey-Thompson, M. R. Weis, E. C. Harding, M. Geissel, D. J. Ampleford, G. A. Chandler, J. R. Fein, M. E. Glinsky, M. R. Gomez, K. D. Hahn, et al., “Diagnosing and mitigating laser preheat induced mix in MagLIF,” *Phys. Plasmas* **25**, 112705 (2018).
- ²¹M. Geissel, A. J. Harvey-Thompson, T. J. Awe, D. E. Bliss, M. E. Glinsky, M. R. Gomez, E. Harding, S. B. Hansen, C. Jennings, M. W. Kimmel, et al., “Minimizing scatter-losses during pre-heat for magneto-inertial fusion targets,” *Phys. Plasmas* **25**, 022706 (2018).
- ²²A. J. Harvey-Thompson, A. B. Sefkow, M. S. Wei, T. Nagayama, E. M. Campbell, B. E. Blue, R. F. Heeter, J. M. Koning, K. J. Peterson, and A. Schmitt, “Laser propagation measurements in long-scale-length underdense plasmas relevant to magnetized liner inertial fusion,” *Phys. Rev. E* **94**, 051201 (2016).
- ²³A. J. Harvey-Thompson, A. B. Sefkow, T. N. Nagayama, M. S. Wei, E. M. Campbell, G. Fiksel, P. Y. Chang, J. R. Davies, D. H. Barnak, V. Y. Glebov, et al., “Diagnosing laser-preheated magnetized plasmas relevant to magnetized liner inertial fusion,” *Phys. Plasmas* **22**, 122708 (2015).
- ²⁴P. F. Schmit, P. F. Knapp, S. B. Hansen, M. Gomez, K. D. Hahn, D. B. Sinars, K. J. Peterson, S. A. Slutz, A. B. Sefkow, T. J. Awe, et al., “Understanding fuel magnetization and mix using secondary nuclear reactions in magneto-inertial fusion,” *Phys. Rev. Lett.* **113**, 155004 (2014).
- ²⁵P. F. Knapp, P. F. Schmit, S. B. Hansen, M. R. Gomez, K. D. Hahn, D. B. Sinars, K. J. Peterson, S. A. Slutz, A. B. Sefkow, T. J. Awe, et al., “Effects of magnetization on fusion product trapping and secondary neutron spectra,” *Phys. Plasmas* **22**, 056312 (2015).
- ²⁶W. E. Lewis, P. F. Knapp, S. A. Slutz, P. F. Schmit, G. A. Chandler, M. R. Gomez, A. J. Harvey-Thompson, M. A. Mangan, D. J. Ampleford, and K. Beckwith, “Deep-learning-enabled Bayesian inference of fuel magnetization in magnetized liner inertial fusion,” *Phys. Plasmas* **28**, 092701 (2021).
- ²⁷R. D. McBride and S. A. Slutz, “A semi-analytic model of magnetized liner inertial fusion,” *Phys. Plasmas* **22**, 052708 (2015).

- ²⁸R. D. McBride, S. A. Slutz, R. A. Vesey, M. R. Gomez, A. B. Sefkow, S. B. Hansen, P. F. Knapp, P. F. Schmit, M. Geissel, A. J. Harvey-Thompson, et al., “Exploring magnetized liner inertial fusion with a semi-analytic model,” *Phys. Plasmas* **23**, 012705 (2016).
- ²⁹P. F. Schmit and D. E. Ruiz, “A conservative approach to scaling magneto- inertial fusion concepts to larger pulsed- power drivers,” *Phys. Plasmas* **27**, 062707 (2020).
- ³⁰D. E. Ruiz, P. F. Schmit, D. A. Yager-Elorriaga, M. R. Gomez, M. R. Weis, C. A. Jennings, A. J. Harvey-Thompson, P. F. Knapp, S. A. Slutz, D. J. Ampleford, K. Beckwith, and M. K. Matzen, “Exploring the parameter space of MagLIF implosions using similarity scaling. II. Current scaling,” (placeholder for reference).
- ³¹D. E. Ruiz, P. F. Schmit, M. R. Weis, K. J. Peterson, and M. K. Matzen, “Exploring the parameter space of MagLIF implosions using similarity scaling. III. Rise-time scaling,” (placeholder for reference).
- ³²R. D. McBride, C. A. Jennings, R. A. Vesey, G. A. Rochau, M. E. Savage, W. A. Stygar, M. E. Cuneo, D. B. Sinars, M. Jones, K. R. LeChien, et al., “Displacement current phenomena in the magnetically insulated transmission lines of the refurbished Zaccelerator,” *Phys. Rev. ST Accel. Beams* **13**, 51 (2010).
- ³³M. R. Gomez, R. M. Gilgenbach, M. E. Cuneo, C. A. Jennings, R. D. McBride, E. M. Waisman, B. T. Hutsel, W. A. Stygar, D. V. Rose, and Y. Maron, “Experimental study of current loss and plasma formation in the Zmachine post-hole convolute,” *Phys. Rev. Accel. Beams* **20**, 010401 (2017).
- ³⁴A different partitioning of the liner mass per-unit-length between the two regions is possible.
- ³⁵In Eq. (26), we have assumed that electrons and ions can be described using the same temperature T . This assumption is valid as long as the electron-ion energy exchange time is small compared to the characteristic times for the various phases of a MagLIF implosion; such as, preheat, implosion, and stagnation.
- ³⁶D. D. Ryutov, M. S. Derzon, and M. K. Matzen, “The physics of fast Z pinches,” *Rev. Mod. Phys.* **72**, 167 (2000).
- ³⁷D. D. Ryutov and M. A. Dorf, “Evolution of helical perturbations in a thin-shell model of an imploding liner,” *Phys. Plasmas* **21**, 112704 (2014).
- ³⁸A. Bose, R. Betti, D. Shvarts, and K. M. Woo, “The physics of long- and intermediate-wavelength asymmetries of the hot spot: Compression hydrodynamics and energetics,” *Phys. Plasmas* **24**, 102704 (2017).
- ³⁹R. Nora, R. Betti, K. S. Anderson, A. Shvydky, A. Bose, K. M. Woo, A. R. Christopherson, J. A. Marozas, T. J. B. Collins, P. B. Radha, et al., “Theory of hydro-equivalent ignition for inertial fusion and its applications to OMEGA and the National Ignition Facility,” *Phys. Plasmas* **21**, 056316 (2014).
- ⁴⁰In present-day MagLIF experiments, the laser pulse is ~ 6 -ns long compared to the ~ 100 -ns duration of the implosion. Due to the difference in timescales, it is a good approximation to consider that the preheat energy is delivered instantaneously. However, this approximation is not commonly assumed in more complex, radiation-magnetohydrodynamic models of MagLIF implosions.
- ⁴¹Equation (54) assumes that the trapped α particles instantaneously deposit their energy to the electrons and that the subsequently heated electrons equilibrate instantaneously with the fuel ions. This is a good approximation as long as the characteristic time for these two processes (α -particle slow down and electron-ion equilibration) are small compared to the characteristic fuel-burn time.
- ⁴²M. M. Basko, A. J. Kemp, and J. Meyer-ter Vehn, “Ignition conditions for magnetized target fusion in cylindrical geometry,” *Nucl. Fusion* **40**, 59 (2002).
- ⁴³S. Atzeni and J. Meyer-ter Vehn, *The Physics of Inertial Fusion: Beam-Plasma Interaction, Hydrodynamics, Hot Dense Matter*, International Series of Monographs on Physics (Oxford University Press Inc., New York, 2009).
- ⁴⁴S. I. Braginskii, in *Reviews of Plasma Physics* (Consultants Bureau, New York, 1965), pp. 1–56.
- ⁴⁵O. A. Hurricane, S. A. MacLaren, M. D. Rosen, J. H. Hammer, P. T. Springer, and R. Betti, “A thermodynamic condition for ignition and burn-propagation in cryogenic layer inertially confined fusion implosions,” *Phys. Plasmas* **28**, 022704 (2021).
- ⁴⁶R. Betti, P. Y. Chang, B. K. Spears, K. S. Anderson, J. Edwards, M. Fatenejad, J. D. Lindl, R. L. McCrory, R. Nora, and D. Shvarts, “Thermonuclear ignition in inertial confinement fusion and comparison with magnetic confinement,” *Phys. Plasmas* **17**, 058102 (2010).
- ⁴⁷D. D. Ryutov, “Characterizing the plasmas of dense Z-pinches,” *IEEE Trans. Plasma Sci.* **43**, 2363 (2015).
- ⁴⁸A. L. Velikovich, J. L. Giuliani, and S. T. Zalesak, “Magnetic flux and heat losses by diffusive, advective, and Nernst effects in magnetized liner inertial fusion-like plasma,” *Phys. Plasmas* **22**, 042792 (2015).
- ⁴⁹H. S. Bosch and G. M. Hale, “Improved formulas for fusion cross-sections and thermal reactivities,” *Nucl. Fusion* **32**, 611 (1992).
- ⁵⁰These circuit parameters are roughly representative to those used in Ref. 32. However, the capacitance C is set to a small value in this paper. Ref. 32 shows that the capacitor only affects the early rise of the delivered currents to the loads.
- ⁵¹J. Katzenstein, “Optimum coupling of imploding loads to pulse generators,” *J. Appl. Phys.* **52**, 676 (1981).
- ⁵²Note that, when evaluating the dimensionless quantities for the energy gain/loss mechanisms in Eqs. (85)–(89), we have used the characteristic plasma conditions for the preheat and stagnation phases given in Table II. In particular, we have used the characteristic timescale Δt of the implosion stage considered, not the characteristic timescale t_φ of the voltage source.
- ⁵³S. A. Slutz and R. A. Vesey, “High-gain magnetized inertial fusion,” *Phys. Rev. Lett.* **108**, 1139 (2012).
- ⁵⁴S. A. Slutz, “Scaling of magnetized inertial fusion with drive current rise-time,” *Phys. Plasmas* **25**, 082707 (2018).
- ⁵⁵It is commonly thought that small dimensionless parameters (much smaller than 0.1) describe physical effects that can be neglected. Therefore, such parameters are considered non-essential. It is worth noting here that large dimensionless parameters (much greater than 10) can also be considered non-essential since these parameters could be replaced by their reciprocals, which are also dimensionless and would be small.
- ⁵⁶B. L. Bures and M. Krishnan, “An alternative scaling model for neutron production in Z-pinch devices,” *Phys. Plasmas* **19**, 112702 (2012).
- ⁵⁷A. L. Velikovich, R. W. Clark, J. Davis, Y. K. Chong, C. Deeney, C. A. Coverdale, C. L. Ruiz, G. W. Cooper, A. J. Nelson, J. Franklin, et al., “Z-pinch plasma neutron sources,” *Phys. Plasmas* **14**, 022701 (2007).
- ⁵⁸T. J. Awe, C. A. Jennings, R. D. McBride, M. E. Cuneo, D. C. Lamppa, M. R. Martin, D. C. Rovang, D. B. Sinars, S. A. Slutz, A. C. Owen, et al., “Modified helix-like instability structure on imploding z-pinch liners that are pre-imposed with a uniform axial magnetic field,” *Phys. Plasmas* **21**, 056303 (2014).
- ⁵⁹T. J. Awe, R. D. McBride, C. A. Jennings, D. C. Lamppa, M. R. Martin, D. C. Rovang, S. A. Slutz, M. E. Cuneo, A. C. Owen, D. B. Sinars, et al., “Observations of modified three-dimensional instability structure for imploding z-pinch liners that are pre-magnetized with an axial field,” *Phys. Rev. Lett.* **111**, 235005 (2013).
- ⁶⁰V. I. Oreshkin, “Thermal instability during an electrical wire explosion,” *Phys. Plasmas* **15**, 092103 (2008).
- ⁶¹K. J. Peterson, D. B. Sinars, E. P. Yu, M. C. Herrmann, M. E. Cuneo, S. A. Slutz, I. C. Smith, B. W. Atherton, M. D. Knudson, and C. Nakhleh, “Electrothermal instability growth in magnetically driven pulsed power liners,” *Phys. Plasmas* **19**, 092701 (2012).
- ⁶²T. J. Awe, E. P. Yu, M. W. Hatch, T. M. Hutchinson, K. Tomlinson, W. D. Tatum, K. C. Yates, B. T. Hutsel, and B. S. Bauer, “Seeding the explosion of a high-current-density conductor in a controlled manner through the addition of micron-scale surface

- defects,” *Phys. Plasmas* **28**, 072104 (2021).
- ⁶³K. J. Peterson, E. P. Yu, D. B. Sinars, M. E. Cuneo, S. A. Slutz, J. M. Koning, M. M. Marinak, C. Nakhleh, and M. C. Herrmann, “Simulations of electrothermal instability growth in solid aluminum rods,” *Phys. Plasmas* **20**, 056305 (2013).
- ⁶⁴E. P. Yu, T. J. Awe, K. R. Cochrane, K. C. Yates, T. M. Hutchinson, K. J. Peterson, and B. S. Bauer, “Use of hydrodynamic theory to estimate electrical current redistribution in metals,” *Phys. Plasmas* **27**, 052703 (2020).
- ⁶⁵B. B. Pollock, *et al*, “Experimental demonstration of ignition-scale MagLIF preheat in gas pipe targets at the National Ignition Facility,” to be submitted.
- ⁶⁶Y. B. Zel’dovich and Y. P. Raizer, “*Physics of Shock Waves and High-Temperature Hydrodynamic Phenomena*,” (Academic, New York, 1966), pp 45–52.